3-D mapping of permeable structures affecting a deep granite basement using isotropic 3C VSP data

Joachim Place, Judith Sausse, Jean-Michel Marthelot, Marc Diraison, Yves Géraud, Charles Naville

Geophysical Journal International

Geophys. J. Int. (2011) **186,** 245–263 doi: 10.1111/j.1365-246X.2011.05012.x

3-D mapping of permeable structures affecting a deep granite basement using isotropic 3C VSP data

Joachim Place,[1,*] Judith Sausse,[2] Jean-Michel Marthelot,[1] Marc Diraison,[1] Yves Géraud[1] and Charles Naville[3]

[1] *Institut de Physique du Globe de Strasbourg, IPGS – UMR* 7516, *Université de Strasbourg/EOST, CNRS,* 1 *rue Blessig,* 67084 *Strasbourg cedex, France. E-mail: joachim.place@eifer.org*

[2] *Département Géosciences, UMR CNRS* 7566 *G2R Géologie et Gestion des Ressources Minérales et Energétiques, BP* 70239, 54506 *Vandœuvre-lès-Nancy, France*

[3] *IFP, Division Géologie – Géochimie,* 1–4 *avenue de Bois Préau,* 92582 *Rueil-Malmaison, France*

Accepted 2011 March 8. Received 2011 February 28; in original form 2010 July 28

SUMMARY

This paper illustrates the efficiency of vertical seismic profiling (VSP) for the investigation of dipping and hydraulically conductive structures affecting a granitic basement covered by sediments. A three-component (3C) VSP data set has been acquired in the GPK1 and EPS1 wells of the Soultz-sous-Forêts enhanced geothermal system (EGS) located within the Upper Rhine Graben (URG). Our study focuses on the isotropic processing of profiles acquired with vertical vibrator *P* and their subsequent interpretation. Mainly *P*–*S* converted reflections are identified from the analysis of the 3C records. These *P*–*S* conversions occur on steep permeable faults that are positioned in space by traveltime modelling. These faults cut the granite basement in several hectometric-scale blocks, and represent the main fluid paths between the boreholes. These faults are thought to be inherited from late Variscan and Alpine deformation periods, reactivated by the current stress field. When properly processed and interpreted, VSP allow the scale gap between surface and borehole data to be bridged.

Key words: Downhole methods; Hydrothermal systems; Fracture and flow; Wave propagation.

1 INTRODUCTION

One of the main problems encountered in the exploitation of fractured reservoirs, especially in crystalline basements, is the lack of geological knowledge at the reservoir scale (Schutter 2003; Luthi 2005; Al-Ali *et al.* 2009). Surface geophysical techniques allow the investigation of the largest structures in a reservoir, but their restricted resolutions prevent their efficiency at lower scales. Coring and borehole imaging provide local and non-exhaustive structural data. Extrapolation of these small-scale fractures at reservoir scale is problematic. Linking borehole data and surface data is complex, but it is necessary to help understanding structural and hydraulic features of fractured media (Tirén *et al*. 1999; Hesthammer & Fossen 2003; Newman *et al.* 2008).

In the framework of the industrial exploration of the Upper Rhine Graben (URG) for geothermal energy, several enhanced geothermal systems (EGS) are being developed at Soultz-sous-Forêts (Alsace), Landau (Rhineland-Pfalz) and Bruchsal (Baden-Württemberg). The Soultz-sous-Forêts site is located in the northeastern part of France (Fig. 1a). This geothermal pilot plant was initiated in the 1980s to develop an artificial heat exchanger in the deep crystalline rocks of the URG (Gérard *et al*. 1984; Gérard & Kappelmeyer 1987). This area was selected because (i) a high geothermal gradient is located at the Soultz-sous-Forêts Horst; (ii) tectonic structure networks activated mainly in late Variscan times, tertiary extension and more recent strike-slip movements were supposed to affect the hot crystalline basement and (iii) the geology of the sedimentary cover is well-documented thanks to many decades of oil exploitation in the Merkwiller-Péchelbronn reservoirs.

The crystalline basement of the Rhine Graben area was formed by the collision of large Variscan domains (Eisbacher *et al*. 1989; Franke 2006; Édel & Schulmann 2009). Major thrusts and suture zones such as the Vittel-Lalaye-Lubine-Baden-Baden fault zone delimiting the Saxothuringian and the Moladanubian domains, and the Tepla Suture trend NE–SW to ENE–WSW (Fig. 1a). A porphyritic granite intruded by an underlying 2-mica microgranite constitute the Soultz-sous-Forêts basement. They were emplaced in Carboniferous times at 334.0 +3.8/−3.5 Ma and 327 ±7 Ma, respectively (Cocherie *et al.* 2004), during the transition between collision and collapse tectonics of the Variscan orogeny. The collapse occurred until Permian times, forming basins trending NE–SW to ENE–WSW (Ziegler *et al.* 2006). Large brittle and ductile

*Now at: EIfER-European Institute for Energy Research, Emmy-Noether-Straße 11, 76131 Karlsruhe, Germany

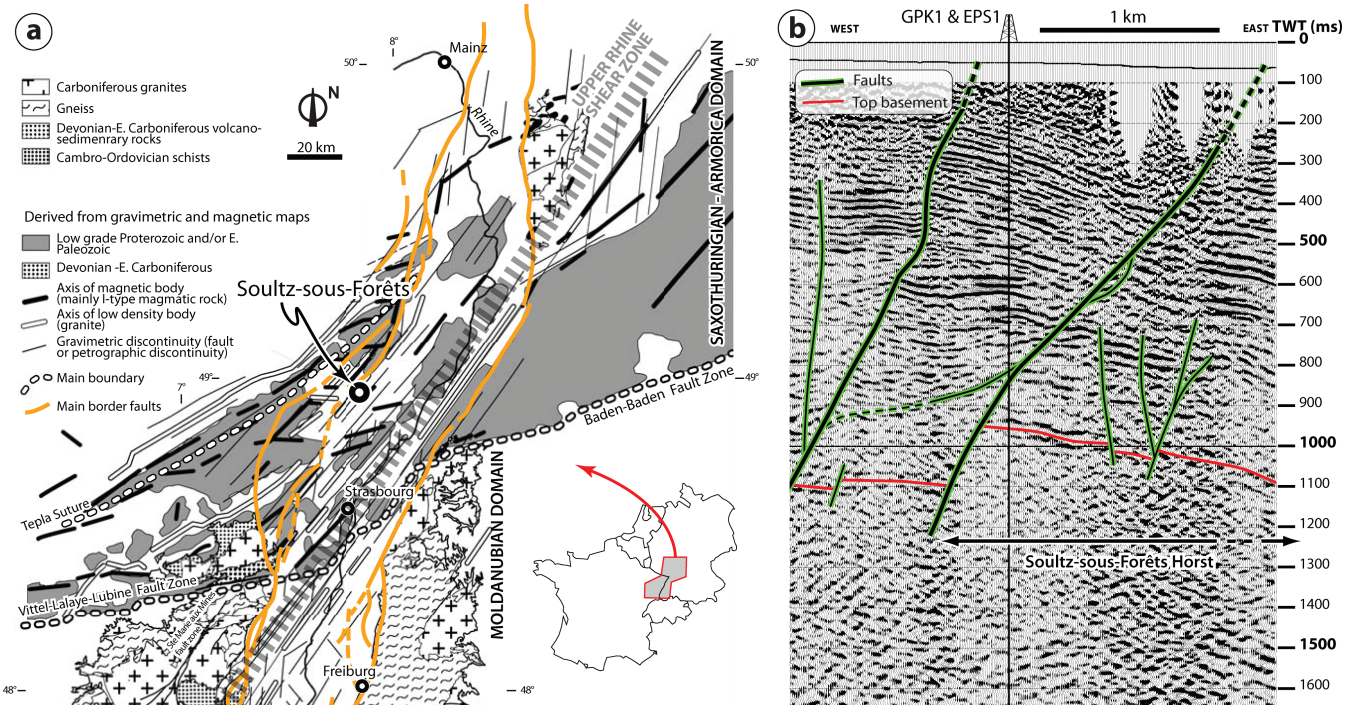

Figure 1. (a) Position map of the Soultz-sous-Forêts EGS within the Upper Rhine Graben, illustrating the variscan inheritance (modified after Édel *et al*. 2007; Édel & Schulmann 2009). (b) E–W oriented seismic reflection profile in the vicinity of the Soultz-sous-Forêts geothermal site exhibiting a typical 'seismic fog' within the basement (modified after Place *et al*. 2010).

strike-slip faults mainly oriented NNE–SSW to ENE–WSW and NW–SE were activated more or less contemporaneously with the development of these basins (Arthaud & Matte 1975).

Mesozoic evolution was quieter; a Liassic slight reactivation of NE–SW faults due to the break-up of Pangea is reported by Edel *et al.* (2007). Major post-Variscan deformations occurred in the Tertiary, with compression tectonics forming Alpine orogenes and extensional regimes developed through Europe (European Cenozoic Rift System); the relations between these two processes are still debated (Ziegler 1992; Dèzes *et al.* 2004; Bourgeois *et al*. 2007). The formation of the Rhine Graben is attributed to a polyphased history brought about by the Eocene N–S compression responsible for a slight localized subsidence, a main E–W extension phase in Rupelian and both transpressional and transtensional tectonics due to Chattian NE–SW compression, then turning NW–SE since the Oligo–Miocene transition (Villemin & Bergerat 1987; Schumacher 2002). Major Oligocene normal faults controlling the deposition of sediments were submeridian. The reactivation of Palaeozoic trends is obvious, although the timing and role of families of faults are still under discussion (Schumacher 2002; Édel *et al.* 2007).

At the present time, three deep geothermal wells reach 5000 m depth in the Soultz-sous-Forêts basement and allow access to temperatures of ca. 200°C (Genter *et al.* 2010). A set of older and less deep wells is also available, such as GPK1 and EPS1, which are studied in this paper. In spite of the large amount of data acquired both at the surface and at depth, fault patterns and deep fluid flow paths within the granitic basement are still poorly understood:

(i) Drilling and logging data and subsequent hydraulic tests (Jupe *et al.* 1994; Genter *et al.* 1995; Jung *et al.* 1995; Evans *et al.* 2005a; Dezayes *et al.* 2010) showed that the main fluid inflows and outflows in the geothermal boreholes occur at depth levels where fractured zones are intersected. From this observation, numerous studies attempted to investigate the structural network in the vicinity of the wells. Borehole wall imaging resulted in the recognition of numerous highly dipping fractures. However, these methods provide local information and are not appropriate to investigate the orientation and extension of the fractures at the reservoir scale (see among others Dezayes 1995). In addition, by comparing such fracture data and cores, Genter *et al.* (1997) showed that even in the best cases, only 50 per cent of fractures could be detected in the wells.

(ii) On a larger scale, seismic reflection (Fig. 1b) and conventional processing of walkaway and vertical seismic profiling (VSP) are not able to delineate steep structures (Dylikowski 1985; Cautru 1989; Beauce *et al.* 1991). Even the contact between the sediments and the basement is discontinuously imaged. *P*- and *S*-wave velocities and hodograms have been used to track velocity variations and *S*-mode wave splitting from VSP data acquired in 1993 in the GPK1 and EPS1 wells, before and after massive water injection. These techniques revealed mainly a heterogeneous structure in the deep part of the GPK1 borehole (~3500 m) that may be related to a fault (Le Bégat *et al.* 1994).

Between these two ranges of scales, only the analysis of microseismic activity recorded during hydraulic stimulations provided some information: the evolution of the seismicity in terms of location, time and signatures (Beauce *et al*. 1991; Evans *et al*. 2005b; Cuenot *et al*. 2006; Bourouis & Bernard 2007; Dorbath *et al*. 2009) or velocity anomalies by tomography (Jones 1993; Charléty *et al*. 2006) allowed researchers to recognize some decametric to kilometric fault zones in the vicinity of the wells. Although the structural control and the fluid involvement in microseismic processes is not clearly understood (Cornet *et al*. 1997; Kohl *et al*. 2006), seismicity results are of major importance in gaining information about the extension and orientation of faults. Structural reservoir modelling benefits from microseismic clouds to extrapolate at the reservoir

scale the fault zones intersected by the boreholes (Sausse *et al*. 2010). Thus, passive and active seismic studies are worth developing for structural geology applications at the reservoir scale.

In other crystalline basements, several reflection seismic studies showed good results for the investigation of gently dipping tectonic or petrographic structures in igneous rocks (Green & Mair 1983; Spencer *et al*. 1993; Milkereit *et al*. 1994; Juhlin 1995; Miao *et al*. 1995). Such structures are not detected within the basement in Soultz-sous-Forêts on similar data (Fig. 1b). Large steeply dipping reflectors have been depicted by seismic reflection on outcropping crystalline rocks (Juhlin *et al*. 2010), but similar results cannot be expected in our case study due to the thickness of the sedimentary cover (∼1.5 km) and the required resolution (hectometric spacing of the faults).

Seismic surveys with specific geometries are better adapted to crystalline basements. A VSP is a field measurement procedure in which the seismic source is activated at a fixed surface position and the seismic signal is recorded by sensors located in a well at successive depth levels (Mari *et al.* 2003). In this way, seismic events such as reflections or refractions generated by structures that may present a high dip value can be recorded and analysed for structural characterization. For example, 3-D fault mapping has been obtained by Emsley *et al*. (2007) in a fractured carbonate reservoir from the analysis of reflections on VSP data. Cosma *et al*. (2001) and Martí *et al*. (2006) produced similar delineations in crystalline settings. Both of these studies provide structural images at reservoir scale, but only some of the faults are believed to be detected owing to features not completely understood such as the thickness of the fault zones, the porosity distribution, the fluid content. Nevertheless, these convincing results encouraged the full processing of a three-component (3C) VSP data set acquired at the Soultz-sous-Forêts EGS, even if the crystalline geothermal reservoir is hidden by a thick (∼1400 m) sedimentary cover (Fig. 1b). This paper illustrates some isotropic processing and interpretation methods of such 3C VSP data, targeting the 3-D mapping of steep faults affecting the granitic basement at the geothermal reservoir scale. In the following sections, all depth values are measured depths from well heads.

2 STATUS OF THE VSP DATA USED IN THIS STUDY

In the early days of the Soultz-sous-Forêts EGS project, a first well called GPK1 was drilled in 1987 down to 2002 m, and deepened in 1992 down to 3590 m depth; in this vertical borehole, the granite is encountered at 1377 m. Another exploration well, called EPS1, was cored from 930 to 2227 m through the basis of the sedimentary cover and the top of granite reached at 1417 m. In its lower part, the deviation of the well is about 23°, making drilling operations stop.

In 1993, a VSP survey was carried out in GPK1 and EPS1 to characterize the fracturation in the vicinity of these wells (Le Bégat *et al.* 1994). The VSP data set was acquired in Vibroseis using an AMG VSP tool, type 'GEOLOCK-S (or SLIM)', with three orthogonal components (14 Hz geophone allowing substantial tilt). One of the geophones was vertically oriented, the others were horizontal. Data were loaded with a Geosource DSS10 recorder. A vertical vibrator was used to preferentially generate *P* waves (Fig. 2a); each run was recorded with two horizontal vibrators (in orthogonal positions), with at least one in an offset position from the well to allow the orientation of horizontal components of the VSP tool. The VSP data were already pre-processed and available in SEG-Y format (2 ms sampling rate, 4 s length). They consist of 3C traces oriented in geographical coordinates, with 40 levels per VSP set (2700–3480 m with 20 m spacing in GPK1 and 1790–2180 m with 10 m spacing in EPS1). This study focuses only on the profiles acquired with the *P* vibrators.

3 ISOTROPIC 3C DATA PROCESSING

The direct arrivals recorded in GPK1 after pre-processing obtained from certain source positions are clearly disturbed by some other arrivals (Fig. 2b). The processing detailed below and in Fig. 3 aims at extracting these secondary arrivals to attempt an imaging of potential structures within the granite.

3C processing requires that the three geophone components of seismic data are recorded by a borehole VSP tool insuring a reasonably isotropic mechanical coupling of the sensors to the

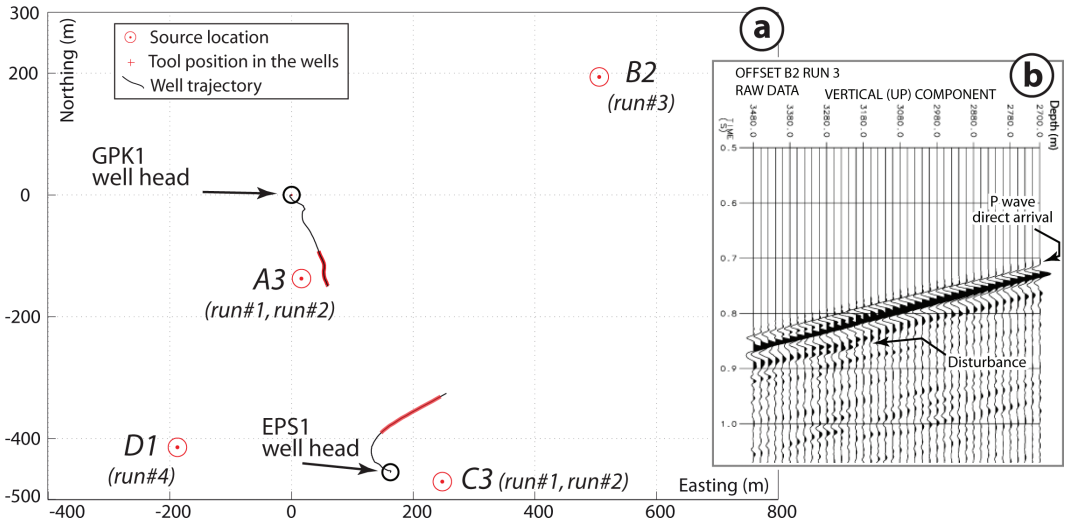

Figure 2. (a) Position map of the *P*-seismic source position during the 1993 VSP survey and trajectory of the GPK1 and EPS1 wells. GPK1 well-head UTM coordinates are (Easting 416934.67; Northing 5420570.09). A3 and C3 are considered to be zero offset VSPs for GPK1 and EPS1, respectively. Other locations provide offset VSPs. (b) Example of raw VSP data (vertical component of the offset VSP B2 run 3). The *P*-wave direct arrival looks disturbed at depth, likely due to an additional seismic event linked to the presence of a structure.

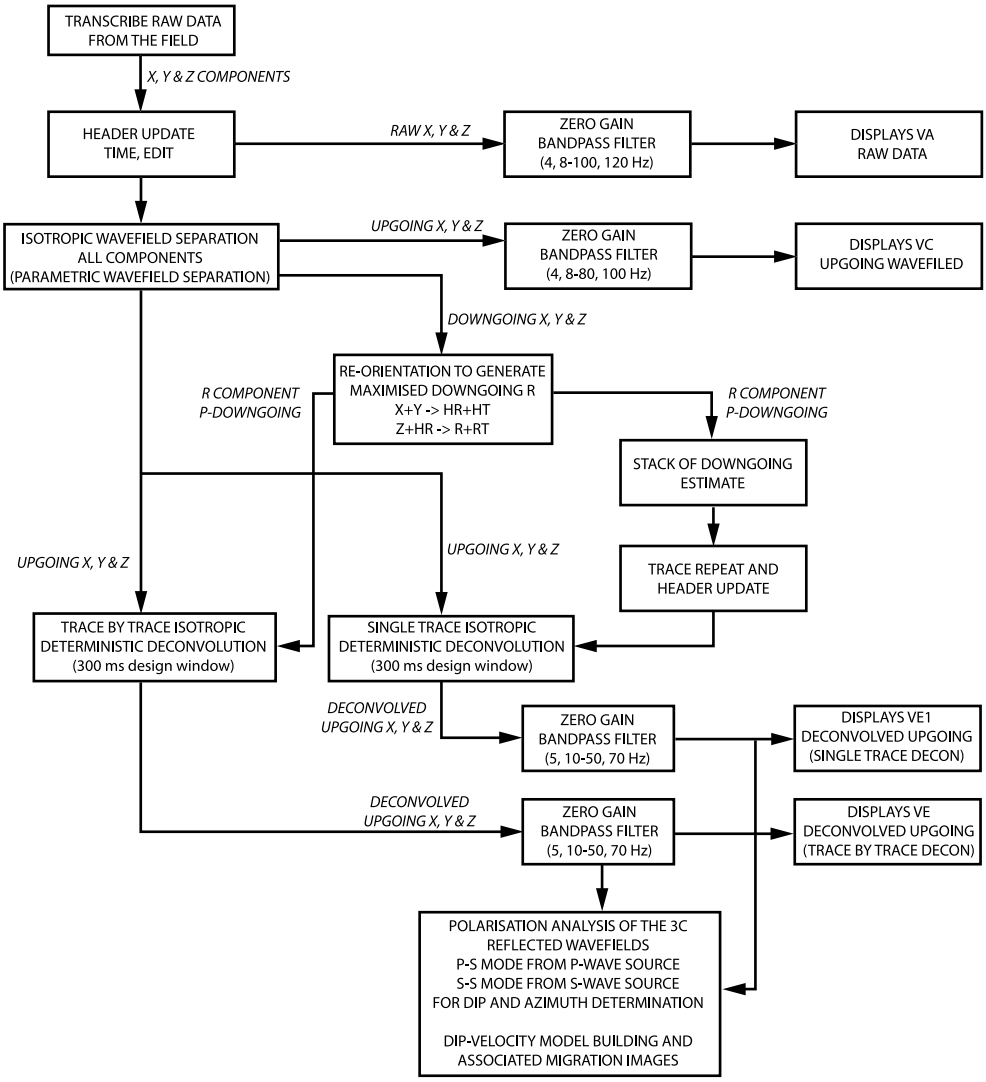

Figure 3. Processing route of the VSPs, consisting mainly in wave field separation, deconvolution and further steps like migration or polarization analysis.

borehole wall. Isotropic 3C processing indicates that the three component signals from any tool station are processed in the same way at the same time, through the whole processing sequence, so that the relative amplitudes of the desired events are preserved. The spatial polarizations of the seismic events remaining after processing are kept and can be accurately determined. The discrimination between *P*- and *S*-wave mode events is much more reliable when using isotropic 3C processing in comparison with single component processing. The isotropic 3C processing procedures can be time variant.

After editing and formatting the data, the processing consisted of an isotropic separation of the upgoing and downgoing wavefields by a parametric separation routine (Fig. 3). Then, an isotropic deconvolution of the upgoing wavefield was performed using an operator derived from the downgoing *P*-wave estimate. This method yields a better precision to discern the different waves especially when they arrive close together in time. Filters have been applied post-separation and post-deconvolution; all filters applied are zero gain, zero phase weighted Ormsby bandpass filters. Finally, the *P*-wave direct arrival has been muted.

This sequence has been applied to VSPs acquired in GPK1 and EPS1 with *P* source positioned in four sites at the surface (Fig. 2a). Sources A3 and C3 are considered as zero-offset VSPs relative to GPK1 and EPS1, respectively; the two other locations (B2, D1) correspond to offset VSPs for the two wells. VSPs were acquired in four runs, thus several VSPs are available for some source locations. The processing sequence has been applied to nine of these VSPs.

Kirchhoff migration—assuming a pressure signal measured by a pressure sensor—was also tried on some data to help interpretation. Velocities were derived from zero offset records. The aim of such a processing is to replace in depth and distance the seismic events that are initially represented in depth and time.

4 INTERPRETATION

Fig. 4 presents the VSPs from GPK1 and EPS1 data sets after processing. Signals appearing more or less coherent through numerous depth levels are observed. Some arrivals such as PS1 and PS2-lowseg are partially blended with the *P* direct arrival, which has been muted. Thus, these events are linked to the presence of structures which are intersected by the well at the depth where the events arrive at the same time with the *P* direct arrival. Other arrivals (PS2-uppseg, PS3, PS4, PS5, PS6) occur much later than the *P* direct arrivals

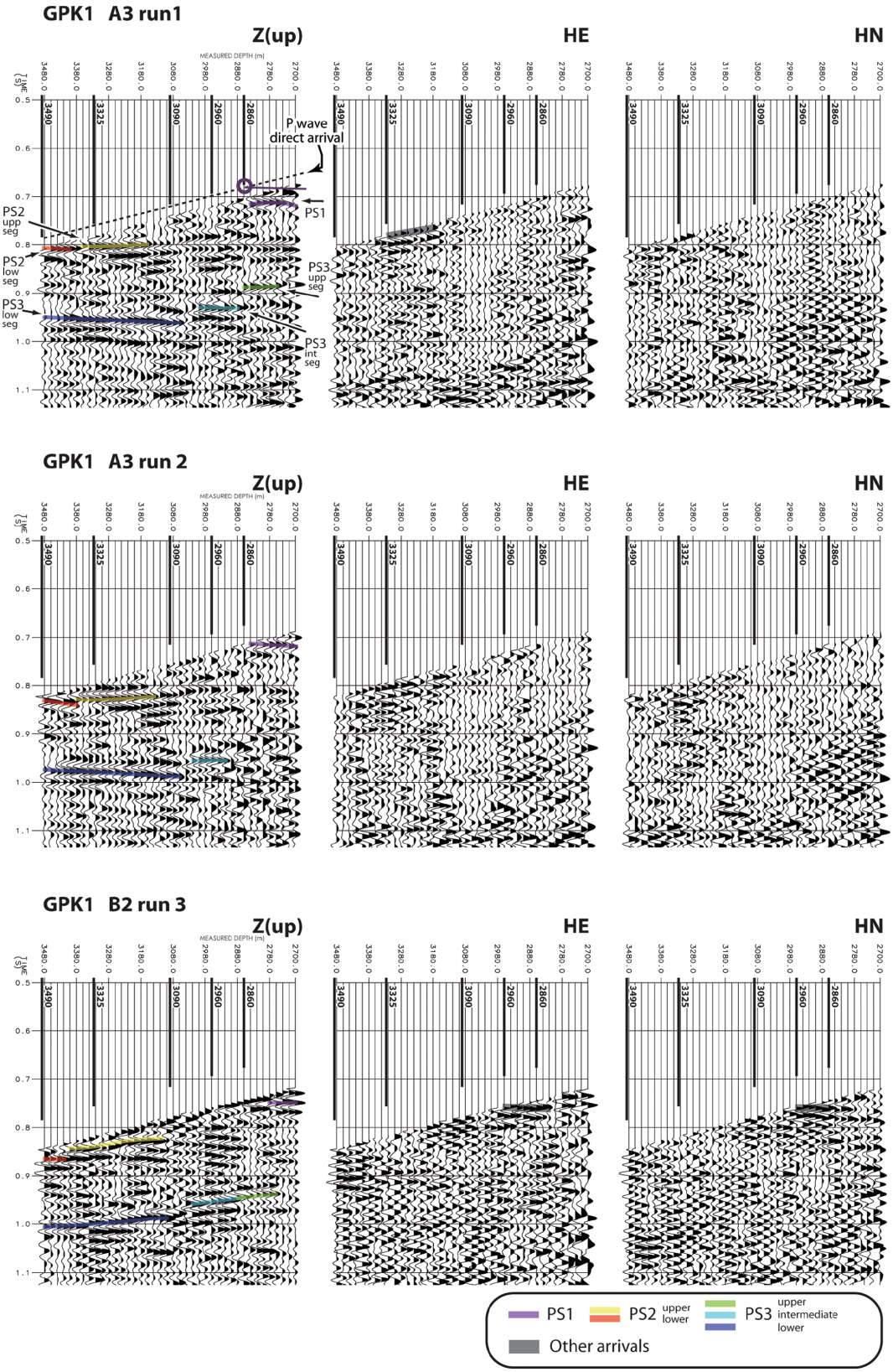

Figure 4. Three component signals of VSPs acquired at Soultz-sous-Forêts in 1993 after isotropic processing (regarding EPS1, only relevant components of VSP are represented). HE and HN are, respectively, horizontal East and North components; *Z* is the vertical (up) component. Seismic arrivals recorded mainly in the vertical components and observed at similar time–depth curves on several profiles are interpreted as *P*–*S* reflections occurring on faults. Other arrivals appearing erratically on horizontal components are attributed to *P*–*P* reflections. Thick black lines highlight depth levels where fluid flow anomalies associated to faults are reported in the boreholes (2860, 2960, 3090, 3325, 3490 m in GPK1, 2070, 2160 m in EPS1, see references in text).

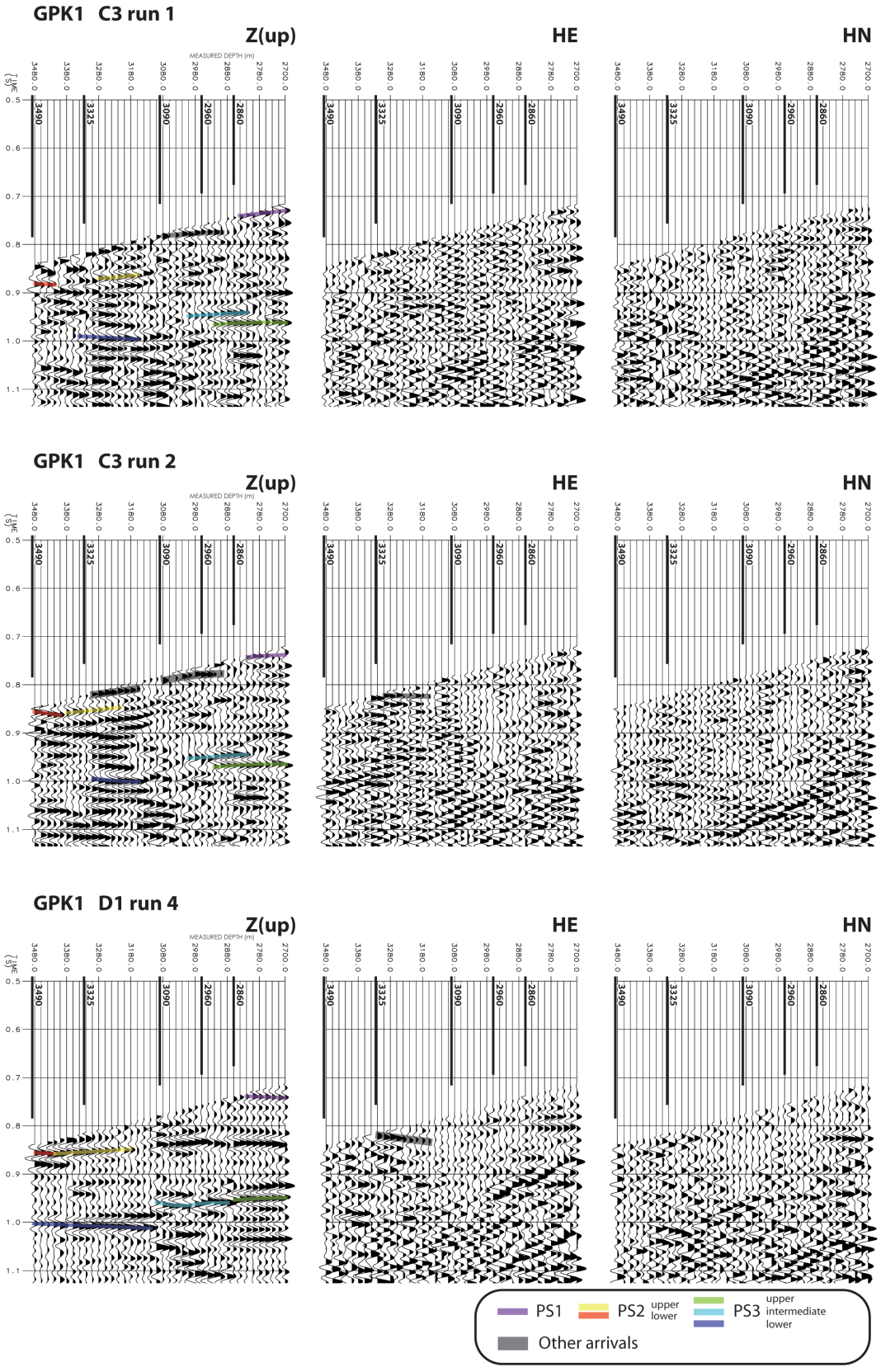

Figure 4. (*Continued.*)

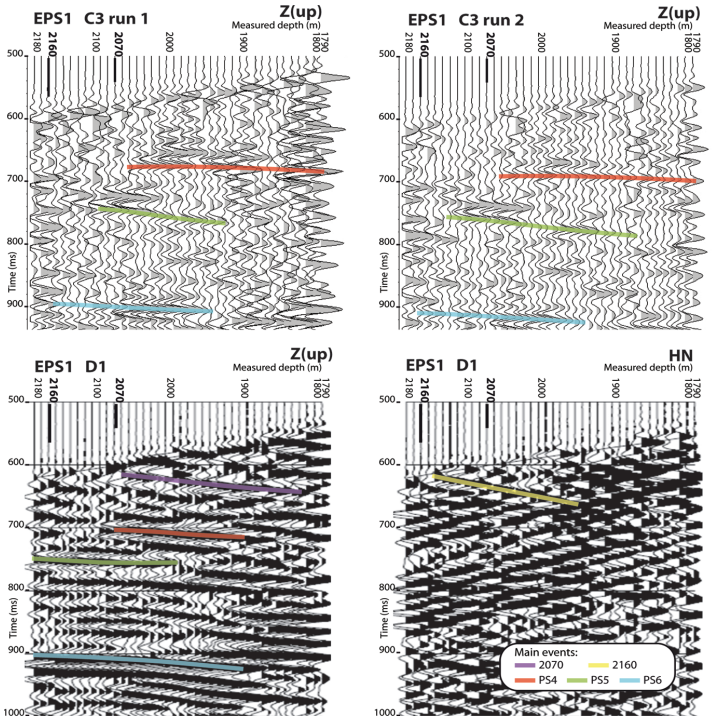

Figure 4. (*Continued*.)

(Fig. 4), thus they correspond to structures that are not encountered by the acquisition boreholes.

In general in borehole seismic measurements, the signals from the horizontal components are known to be less reliable than the vertical one. Nevertheless, in this data set they may also be considered with confidence, because of the rather low noise level and the clear arrivals exhibited in particular using the *S* sources of the data set (not shown here). The seismic events PS1–PS6 appear clearly on the vertical component (*Z*) and are invisible on horizontal components (HE and HN, Fig. 4). This feature indicates that the energy of the waves is vertically polarized. These events arrive after the *P* direct wave such as shown in Fig. 2(b), and before the *S* direct waves time–depth curves measured on *S*-source VSP data (not shown here). Thus, these arrivals cannot be direct waves from the source located at the surface down to the tool at depth; they are surely deviated by structures affecting the granite around the borehole. As a consequence, the rays representing their propagation cannot be vertical; they should exhibit low dip angles (Fig. 5). Such a wave propagating in *P* mode would inevitably show a signal at least on one horizontal component (see dashed line in Fig. 5). As it is not the case, the observed arrivals are *S* waves, vertically polarized and propagating horizontally (continuous black line in Fig. 5). In addition, due to both the relative short arrival time of these *S* waves just after the *P* direct arrival and the much later *S* direct arrival, the events PS1–PS6 cannot be issued from S–S conversions. They are generated by P–S conversions occurring on structures located laterally in the vicinity of the wells (Fig. 5). Other examples of interpretations based on polarity analysis are proposed in Appendix (Fig. A2).

In the example of the PS1 event (Fig. 4, source A3 run1, *Z* component), the intersection between its supposed linear onset (violet line) and the onset of the *P* direct arrival (black dashed line) is located by a violet circle around 2860 m. In the same way, the PS2-low-seg (orange line) intersects the *P* direct arrival around 3500 m, out of the depth range of the records. Major fractured zones have been identified at these levels, in which dip values of small scale fractures range mainly from 50° to 70° (Dezayes *et al.* 2010). Assuming that the structures on which the *P*–*S* conversion occur are roughly planar and present a dip value of 60°, and considering the velocities of *P* and *S* waves measured from the zero offset VSPs, the application of Snell–Descartes' law indicates that if a vertical downgoing *P* wave is converted to an *S* wave on this surface, the resulting *S* wave will propagate almost horizontally (Fig. 5). This confirms the *P*–*S* nature of the arrivals observed on the vertical components of the profiles, and indicates that the elastic mode conversion occurs by reflection. Fractured zones at 2860 and 3490 m presented large amounts of gas and natural brine when drilled (Aquilina & Brach 1995), fluid outlets during hydraulic tests (Evans *et al*. 2005a; Sausse *et al*. 2006), and tube waves when stimulated (Jones 1993). *P*–*S* reflections, and also *S*–*S* reflections, are known to occur in crystalline massifs on fault zones concentrating fluids (Carr *et al*. 1996; Smithson *et al*. 2000; Rabbel *et al*. 2004); this similarity strengthens our interpretation.

The dip value of the faults where reflections occur can be computed with an approach such as presented in Fig. 5. Unfortunately, as no clear signal is recorded by the horizontal geophones it is impossible to derive directly the azimuth of the reflected *S*-wave propagation. An application example of a depth migration has been performed using the *S*-wave velocity on the vertical component of the offset A3 run 2 recorded in GPK1 (compare Figs 4 and 6). Such a picture shows realistic lateral distance of the structures to the well, so that their dip value and their extension can be directly measured. Nevertheless, as the vertical component shows several arrivals without considering azimuth, the migration represents an 'azimuthal spatial stack' of all the arrivals. Thus, a migrated image cannot be considered as a vertical cross-section. Further developments are needed to derive the strike values of the reflectors to arrive at a comprehensible 3-D image.

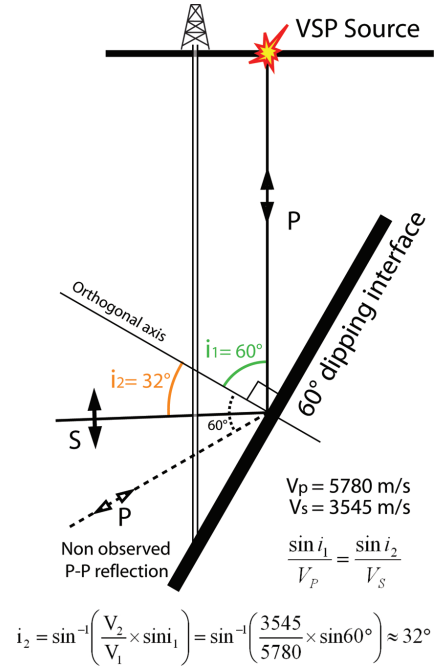

Figure 5. Application of the Snell–Descartes' law on a 60° dipping interface on which a *P*–*S* conversion occurs (a *P*–*P* reflection is represented although it is not observed in our case). Direct downgoing *P* wave is assumed to be vertical (depth scale is not respected, angles are respected). The velocity values are inferred from measurements on zero offset VSP.

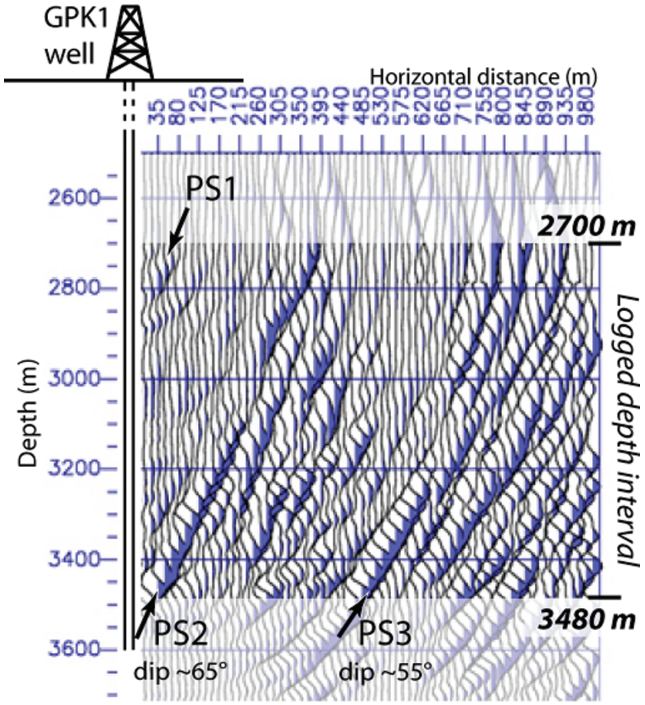

Figure 6. 2-D depth migration of the vertical component signals of the VSP recorded from source A3 run 2 in the GPK1 well using *S*-wave velocity (scale 1:1). Converted *P*–*S* reflections are replaced in space without any consideration of azimuth values of the reflectors.

5 TRAVELTIME MODELLING

For a given tool position in depth, the different sources at the surface do not illuminate the reflector at a same location, inferring differences in arrival times. Based on this principle, the geometrical characterization of the reflectors may be addressed by travelpath and traveltime modelling. Our approach thus consists of a comparison between the observed *P*–*S* traveltimes and the computed *P*–*S* traveltimes subjected to a reflection on a given reflector.

5.1 Modelling tool

Ray travelpaths geometry and associated traveltimes are computed using a Matlab® algorithm, allowing easy 3-D plotting. The program was written in our laboratories for the present purpose. The propagation media is divided into two parts representing the crystalline basement and its sedimentary cover (Fig. 7a). Each part has its own *P*- and *S*-wave velocity values; their contact is a plane with a depth and orientation also defined by the user. Other parameters entered into the program are the source positions and the well trajectory providing the receiver stations. The 3-D trajectory of EPS1 has been considered due to its strong deviation with depth, whereas GPK1 has been supposed to be vertical and positioned at the centre of the logged interval in both easting and northing.

The program computes the geometry of the *P* direct and *P*–*S* reflected travelpaths by taking into account ray refraction at the sediment/basement contact and a reflection with *P* to *S* mode conversion occurring on the intrabasement reflector (Fig.7a). Snell–Descartes' law is thus applied in these computations. The traveltimes are then computed by using the velocity values (Fig. 7c).

If the reflector is intersected by the borehole, reflection event picking is positioned on a reliable signature (maximum amplitude or zero) (Fig. 4). As the times of the picked phase are recorded later than the low amplitude onset of the signal, these values are shifted to make them intersect the *P* direct wave time-depth curve at the depth level where the fault is intersected by the borehole. If the intersection of the fault and the borehole does not occur within the depth interval of the VSP records, the picked traveltimes are shifted with a time value corresponding to a part or a full period of the signal, assuming a good similarity between the wave forms of the different *P*–*S* events. The imaginary intersection depth is assessed by linear downward prolongations of the direct *P* wave and the *P*–*S* reflected wave.

Knowing this depth, the routine is repeated for several orientations of the reflector in defined ranges of dip and dip direction values (Fig. 7a). For each orientation, the residual between observed and computed traveltimes of the *P*–*S* reflection (Fig. 7c) is calculated for each trace from all the exploitable VSPs. Then, the average and the variance of these residuals are considered for each time–depth curves. These results may be plotted for each source in a 3-D surface (Fig. 7b), or in an equivalent way by 2-D plot where sinusoid-shaped curves represent the couples (dip direction; dip) representing the lowest residuals (Figs A1, A3, A4 and A5). The residuals represented in a 3-D space (Fig. 7b) allow the identification of the minimal value that corresponds to the reflector presenting the best orientation to reproduce the observed traveltime curves.

Synthetic VSPs are plotted in time–depth domain to help the comparison with field data (Fig. 7c). 3-D plots exhibiting the ray paths (Fig. 7a) allow some parameters, such as the incidence angle of the *P*–*S* rays at the tool location, the area of the reflector illuminated by the seismic sources, to be estimated.

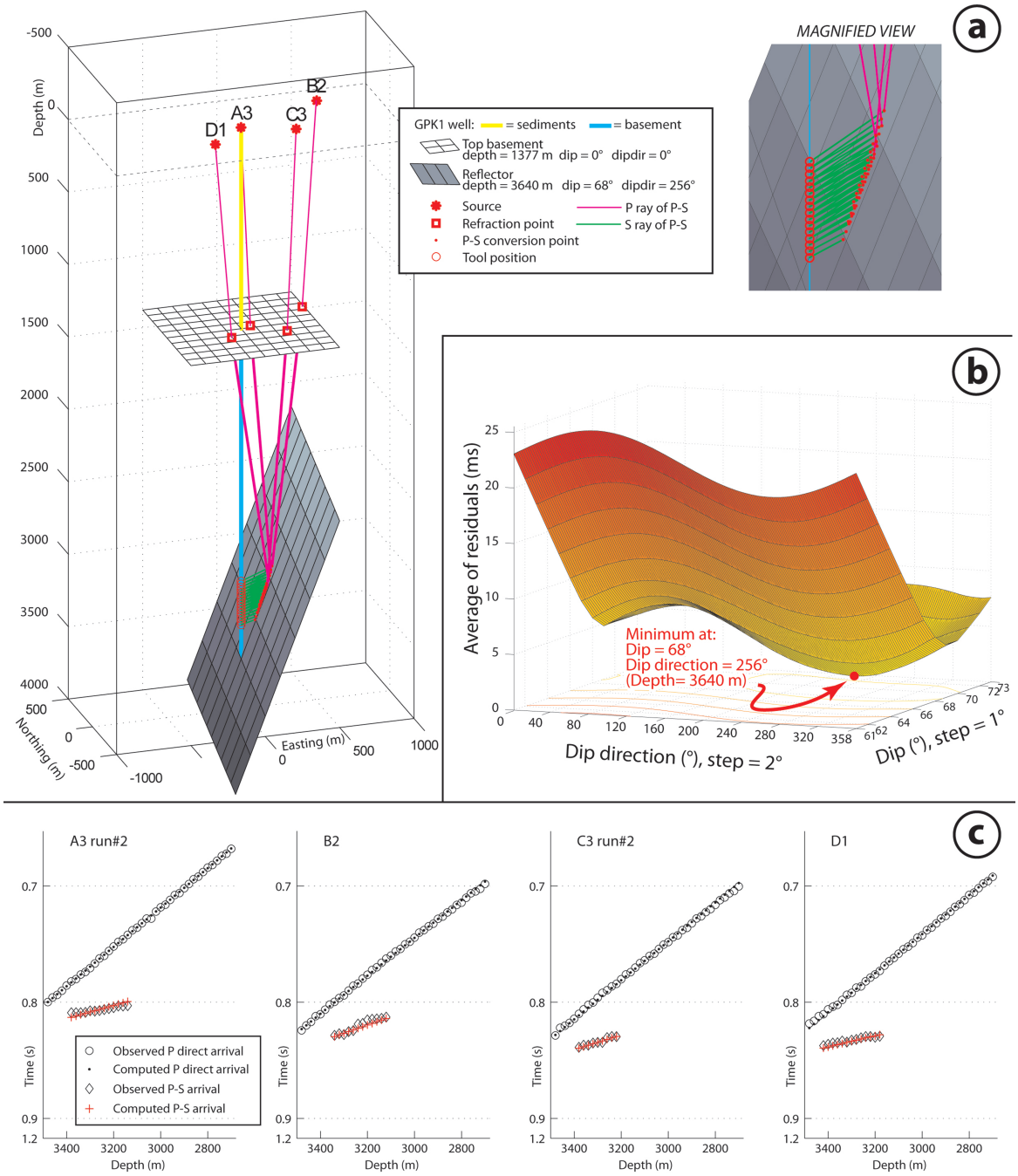

Figure 7. Example of traveltime modelling applied to arrival PS2-upp-seg. (a) 3-D plot showing the geometry of the velocity model and the ray paths. Easting, northing and depth/elevation are given relative to GPK1 well head. Only some examples of *P*–*S* rays are represented for clarity. (b) Residuals of modelling in the field of the investigated orientations. 3-D representation consists in [dip; dip direction; average (through all the VSPs taken into account) of either average or variance of the residuals between observed and modelled traveltimes]. (c) Observed and synthetic arrivals PS2-upp-seg, for the reflector position given in b (N256°E 68°).

5.2 Static corrections

The mean velocity values entered into the model described earlier have been determined from zero offset VSP data: the slope of the *P* direct arrival times depends on the *P*-wave velocity within the granite, and its global time shift depends on the *P*-wave velocity within the cover (Fig. 7c). Nevertheless, these velocity values are not consistent between run 1 and run 2 provided by zero-offset VSPs (source A3 for GPK1, C3 for EPS1). These values do not accurately explain the *P* direct waves recorded on offset VSPs as well, especially regarding the *P*-wave value of the sediments. Thus, the modelling has been applied separately for runs 1 and 2 on the VSPs acquired from the four sources. As results, a total amount of six profiles is available in GPK1 (A3 run 1, A3 run 2, B2, C3 run 1, C3 run 2, D1) and three profiles in EPS1 (C3 run 1, C3 run 2, D1). For each source and each run, static corrections have been introduced so that the computed *P* waves direct arrivals fit the observed one (Fig. 7c).

Table 1. List of reflectors detected by VSP, with orientations deduced from traveltime modelling. Positions of the reflectors in depth are given with respect to GPK1 well head by an imaginary downward vertical continuation of the well, or relatively to ESP1 well head along a vertical axis. Fault zones intersected by the wells are in grey. Three stars (∗∗∗) mean a maximal confidence in the results (see in text for details).

VSP Name	M.D. (m)	T.V.D. (m, below EPS1 well head)	Dip (°)	Dip Dir. (°)	Top (m, T.V.D. below GPK1 or ESP1 well head)	Bottom (m, T.V.D. below GPK1 or EPS1 well head)	Width (m)	Confidence
GPK1-PS1	2860	—	57	295	2700	2860	10	**
GPK1-2960	2960	—	51	045	2840	2960	1	*
GPK1-3090	3090	—	67	255	2845	3090	1	*
GPK1-3325 solution#1	3325	—	63	080	3100	3325	20	*
GPK1-3325 solution#2	3325	—	63	260	3100	3325	20	*
GPK1-PS2-low-seg	3490	—	52	324	3400	3490	10	***
GPK1-PS2-upp-seg	3640	—	68	256	3050	3420	30	***
GPK1-PS3-low-seg	4267	—	59	297	3150	3515	100	*
GPK1-PS3-int-seg	4384	—	63	329	2710	3050	170	**
GPK1-PS3-upp-seg	4362	—	68	150	2650	2910	180	**
EPS1-2070	2070	—	Domain		—	—	—	**
EPS1-2160	2160	—	Domain		—	—	—	**
EPS1-PS4	—	2496	59	297	1820	2090	20	**
EPS1-PS5	—	2655	49	150	2075	2240	60	*
EPS1-PS6 solution#1	—	3937	64	195	2030	2230	150	*
EPS1-PS6 solution#2	—	2650	55	325	2100	2325	150	*

5.3 Results

The modelling has been applied to 14 arrivals depicted in Fig. 4. Six clear arrivals have been selected in the GPK1 data because of their occurrence on the six profiles; the arrival PS2 and PS3 have been split into several segments (PS2-low-seg, PS2-upp-seg, PS3-low-seg, PS3-int-seg, PS3-upp-seg; Fig. 4). The upward prolongation of the PS2 arrival is erratically observed on the available profiles, for this reason only the lower part of this event is considered in this study (Fig. 4).

In a general way, the fit between the synthetic and the observed traveltimes are good. This fact shows that the hypothesis of the planarity of the reflectors is realistic at first order. The results of modelling are gathered in Table 1. Vertical limits and widths of the illuminated areas are measured from 3-D representations such a those presented in Fig. 7a. Confidence in the results is qualitatively assessed on criteria that are: (i) the number of traces in which the event is recorded, (ii) clarity and continuity of the signal through several traces and (iii) occurrence of the event from different sources. The number of sources that illuminate the reflector is not taken into account. Thus, ∗∗∗ in Table 1 indicates an optimum confidence and ∗ a poor confidence. Discussion of the confidence of results is given in the Appendix. Traveltime modelling considering *P–P* reflections results in less steep reflectors. In these cases, the angle of incident rays at tool locations would imply the presence of seismic energy both on the vertical and horizontal components in a similar way as represented in Fig. 5. As no energy is observed, *P–S* conversions on fault zones are confirmed.

Some weaker arrivals are identified around 2960, 3090 and 3325 m. At these depth levels, alteration and fracture density are variable (Sausse *et al*. 2006). Nevertheless, flow anomalies have been reported (e.g. Evans *et al*. 2005a), and they are investigated in this study. For the same reasons, in EPS1, two weak arrivals (2070 and 2160 m) are considered because of flow signatures (Genter *et al*. 1995), in addition to the three clear *P–S* arrivals. These minor arrivals present less clear seismic signals on vertical and, for some of them, on horizontal components. These particular cases require specific interpretations and modelling to derive their orientation. They are commented upon in the Appendix.

6 IMPROVEMENT OF THE RESERVOIR MODEL

The pre-existing 3-D structural model of the reservoir (Sausse *et al*. 2010) has been used to integrate the VSP results. Its structural elements are derived from geological data (Genter *et al*. 1995), well logs (Dezayes 1995; Sausse & Genter 2005; Sausse *et al*. 2006; Dezayes *et al*. 2010), microseismicity recordings (Cuenot *et al*. 2008; Dorbath *et al*. 2009). Some VSP results of the 1993 survey are already integrated in this model, but they are produced from a basic analysis of the arrivals: only dip values and extensions are measured. Strike values are taken from borehole imagery. As new VSP results from this paper consist in more precise positioning of the planes, including azimuth values, the structural model has been updated with the results of Table 1.

The constitution of this static model aims at representing the 3-D network of faults cross-cut by the wells in the deep reservoir as realistically as possible. The gOcad® earth-modelling software environment (Paradigm™, Earth Decision™, Mallet 2002) is used to combine all 3-D data available. Then, a specific FractCar Plug-in is dedicated to the modelling and visualization of 3-D fracture patterns and discrete fracture network (DFN) modelling (Macé *et al.* 2004; Macé 2006). Fracture representation is carried out through a specific point set in which each element is assigned an attribute for the fracture plane orientation, defined by the normal vector n of the plane (in the dip-direction convention). The form of the fracture border is a disc or parallelepiped centered at a specific X Y true vertical depth sub sea (TVDSS) location. The fracture size (or extension) is fixed and tested for each fracture. The output of the DFN model is a synthetic 3-D set of elliptic planes populating a volume around the wells in the reservoir.

(i) Reflectors deduced from PS1 of GPK1 and PS4 of EPS1 arrivals present very similar orientations (Table 1). 3-D geometrical

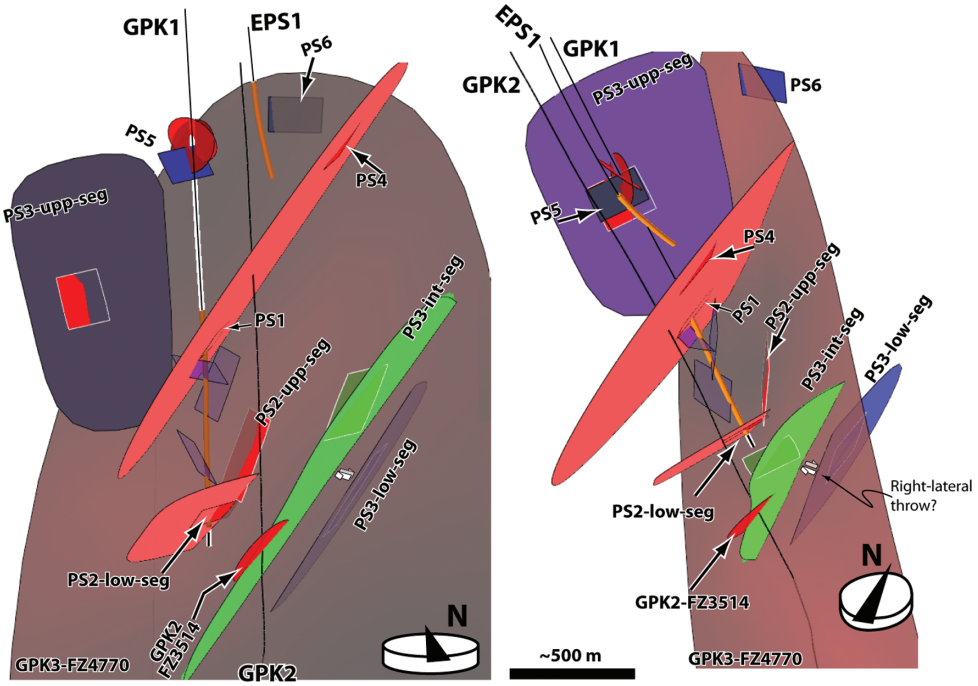

Figure 8. 3-D views of the reflectors in the reservoir model built with gOcad®. Orange sections of GPK1 and EPS1 represent the intervals where the VSP tool was positioned. The large surface in grey-red represents the major fault intersected in GPK3 at 4770 m (GPK3-FZ4770). Small rectangles represent the surfaces effectively illuminated by seismic waves. Larger surfaces are built to represent suspected minimal extent of structures.

representations of these reflectors illustrate that they are aligned in space (Fig. 8). This may be taken as evidence for the delineation of a large fault illuminated by the two GPK1- and EPS1-independent VSP data sets. The resulting surface is represented in orange-red in Fig. 8.

(ii) PS3-int-seg is aligned with a fault zone located at 3514 m in GPK2 (GPK2-FZ3514) (Dezayes *et al*. 2010). Thus, they have been similarly linked (green surface, Fig. 8).

(iii) PS2-upp-seg oriented N256°E 68° (Table 1) may be correlated to the large fault zone GPK3-FZ4770 oriented N234°E 71° that is intersected both in GPK2 and GPK3 (Sausse *et al*. 2010). The solution #1 regarding PS6 very approximately matches both in position and orientation the same large fault. Thus, the solution #2 is rejected. This fault is considered as the major one by Sausse *et al*. (2010), especially on the basis of microseismic clouds (Weidler *et al*. 2002; Charléty *et al*. 2006; Dorbath *et al*. 2009). This work allows to detect the upward prolongation of this big fault, and to connect it to the flower-like structure depicted in seismic reflection data (Fig. 1b). Thus, it is illustrated how a large fault (over 4 km in size) within a basement may be imaged by specific methods, whereas it is indistinctly revealed by seismic reflection.

(iv) The two reflectors PS3-low-seg and PS3-int-seg located on both sides of this big fault have been truncated on it (Fig. 8).

(v) The events PS2-low-seg and PS2-upp-seg appear quite well continuously though the whole data set (yellow and orange lines in Fig. 4). Thus, this is seismic evidence to connect the two reflectors (Fig. 8). As the PS2-upp-seg corresponds to the main fault (GPK3-FZ4770), the reflector of PS2-low-seg has been truncated. By analogy, the surface corresponding to PS3-upp-seg is cut by the big fault (Fig. 8).

The latitude in orientation considered for correlating a seismic reflector with a pre-existing object of the model depends on the confidence indices (Table 1): a surface characterized by a low confidence (∗, e.g. PS6) has more latitude than a surface oriented with confidence (∗∗∗, PS2). After correlation, the resulting large surfaces joining several objects are represented to a reasonable extent regarding the data on which they are based and with respect to the well structural observations (Fig. 8).

The reflector oriented from PS5 intersects GPK1 around 2140 m (Fig. 8). The fault zones neighbouring this intersection are located at 2064 and 2088 m with different orientations from borehole imaging (respectively N039°E 68° and N232°E 67° as dip direction and dip (Genter 1993)). This misfit can be explained by (1) the uncertainties regarding the orientation computed by traveltime modelling (low confidence, see Table 1, and strong sensitivity to the velocity model), and (2) the variable ability of borehole imaging to represent the orientation of a whole fracture zone from the orientation of individual small fractures: for example it is not reliable to distinguish the orientation of a fault zone from conjugated fracture sets developed at lower scale.

7 DISCUSSION

7.1 Review of the traveltime modelling method

As mentioned earlier, if a *P–S* reflection occurs on a reflector not being intersected by the borehole, the depth of the imaginary intersection is computed by basic prolongation. This intersection depth is not precise, but it has only a very low influence on the calculated dip and dip direction values. Anyway, for each source, our seismic methods based on arrival time differences from the same seismic signals are quite robust, because the results are independent of any time filtering or deconvolution applied on the data.

The discrepancies between the observed and modelled traveltimes can be explained: (1) reflections are modelled on planar reflectors, whereas fault zones are known to exhibit dip, dip direction and thickness variations (Childs *et al.* 2009). For instance, the

irregular shape of event PS1 could be explained by a difference in the direction of the downgoing incident *P* wave illuminating differently a structure of complex geometry. This interpretation is in accordance with Huygens' principle. (2) Two media of homogeneous velocities separated by a horizontal plane were considered in the computations (Fig. 7a), whereas the actual velocity field is much more complex. Consequently, the differences regarding the ray paths and the arrival times cannot be perfectly corrected by a basic static correction. (3) The uncertainty of the borehole trajectory is estimated at some tens of metres by Gaucher (1998).

A time delay observed between runs 1 and 2 is still unexplained, even in the acquisition report (Le Bégat *et al.* 1994). As the slope of the time–depth curves of the *P* and *S* direct waves are similar between the runs (for *P* waves, see Fig. 4), the velocities of the waves in the granite are consistent throughout the survey. As variations of the velocities in the sediments along the same routes during the acquisition are difficult to explain, possible variations of acquisition parameters omitted in the field report have to be considered. Thus, static corrections introduced for each source do not only reflect heterogeneities of the velocity field of the Soultz-sous-Forêts area, but also acquisition variations.

The uncertainty regarding the orientation of the reflectors should not exceed $\pm 30^\circ$ and $\pm 5^\circ$ for dip direction and dip, respectively. The fractures oriented from cores and from borehole imagery are oriented with $\pm 15^\circ$ and $\pm 5^\circ$ uncertainties, respectively (Genter *et al.* 1997). As the assessment of the orientation of a whole fault from small-scale individual fractures is, at best, unreliable, the results of the two methods likely occur in the same range of confidence. For example, Sausse *et al*. (2010) illustrated that the orientation of the fault GPK3-FZ4770 is given with minimal ranges of 10° and 15° regarding the dip direction and the dip values in the two wells intersecting the fault, respectively.

The larger the offset of a VSP source, the more different are the time–depth curves of reflections. Numerous far and close offset VSP of various azimuths are thus required to provide a good chance for illuminating the reflectors and constraining their orientation. For example, possible subvertical structures located in the vicinity of acquisition boreholes cannot be properly imaged with the 1993 data because of the poor surface coverage of the sources (Fig. 2a). The low width values of the illuminated area of the reflectors (Table 1) illustrate the lack of profiles shot in a wide range of azimuth and offset values. Numerous sources recorded from different boreholes would allow an overlapping of the illuminated areas on a common reflector. In our study, events PS1 and PS4 are supposed to be linked to a same reflector only from considerations of similar orientations and alignment in space (Table 1 and Fig. 8). Only an overlapping of the illuminated surfaces would definitely validate the assignment of the reflected events to a unique and continuous reflector. In addition to improvements of both the precision and illumination, numerous offset VSPs could provide enough data to attempt a tomographic imaging. Such a processing is restricted to direct arrivals; thus it can be considered as being independent of the secondary reflections used in our study. Thus, two complementary structural characterizations could be carried out with one data set.

3-D vector migration (rather than Kirchhoff migration, Fig. 6) of the data is a direct way to produce 3-D images. However, seismic energy is required on the horizontal components to perform such a development. In the absence of these signatures, traveltime modelling is time-consuming but remains robust. A comparison between the field records (Fig. 4) and 3-D full wave form modelling results would be useful to definitively validate the positions of the reflectors.

P and *S* direct waves recorded in the same VSP survey with *S* sources also exhibit obvious disturbances after pre-processing. After the processing sequence described earlier (Fig. 3), the 3C reflected wavefield exhibits less clear reflected arrivals. Other signal processing should be envisaged for the exploitation of these *S*-wave records.

In Soultz-sous-Forêts, the first studies using such VSP data set were based on typical processing oriented towards reflection and anisotropy (Beauce *et al.* 1991; Le Bégat *et al.* 1994). No clear delineation of individual faults has been produced. Our application of more recent and original isotropic processing, consisting mainly in wave field separation (Cosma *et al*. 2001; Martí *et al*. 2006; Emsley *et al*. 2007), illustrates that reflections occurring on some discrete dipping faults may be detected and separated. Future efforts should be oriented to improve the duration of processing and interpretation sequence that is described here.

7.2 Improvements on the reservoir knowledge

The orientations of the VSP reflectors are represented in Fig. 9. The strikes of the faults are very well gathered in four families around N026°E, N057°E, N120°E and N167°E. They are similar to the directions NNE–SSW (Rhenish), ENE–WSW (Erzgebirgian) and NW–SE that correspond to inherited Palaeozoic strikes in the area (Ziegler 1986; Chorowicz & Deffontaines 1993; Schumacher 2002; Édel *et al*. 2007; Édel & Schulmann 2009) (Fig. 1). Major Tertiary normal faults such as those illustrated in Fig. 1(b) have submeridian strikes, NNE–SSW included (Sittler 1985; Villemin & Bergerat 1987).

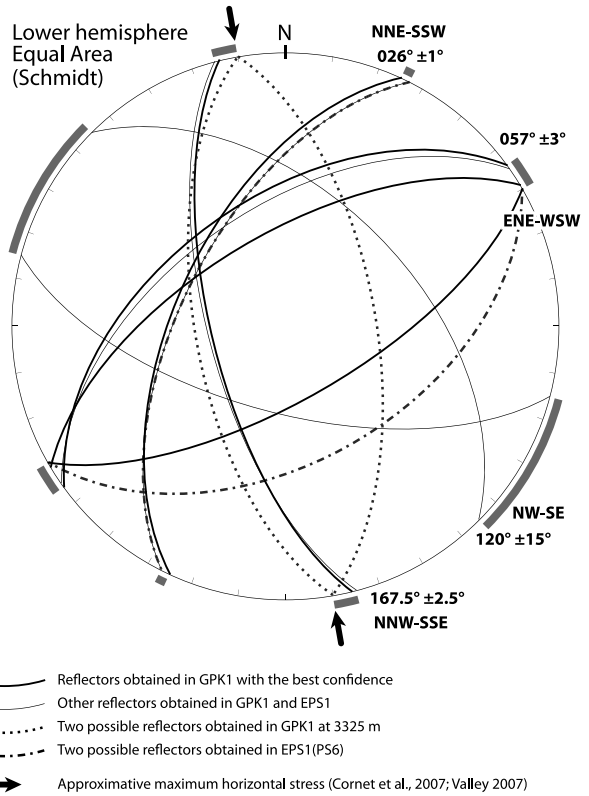

Figure 9. Stereogram showing the orientation of the reflectors mapped from VSP analysis. Reflectors obtained with the best confidence have been restricted to GPK1 (categories ∗∗∗ and ∗∗) because of the poor number of VSPs available in EPS1.

The Permo-carboniferous collapse of the Variscan orogen occurred contemporaneously with strike-slip deformations like NNE–SSW left-lateral strike-slip faults such as the Upper Rhine Shear Zone (Fig. 1) and ENE–WSW and NW–SE right-lateral strike-slip faults (Arthaud & Matte 1975; Ziegler 1986; Franke 2006; Édel *et al*. 2007). Thus, the ∼N026°E and ∼N057°E structures could have been activated in this period. Only a minor reactivation of these faults may be supposed in Liassic times, as this phenomenon has been reported in the southern Vosges (Édel *et al*. 2007). Large-scale folding is also observed prior to the deposition of the Tertiary sediments, involving a system of ENE–WSW trending thresholds (Sittler 1985). The main reactivation period of the Palaeozoic structures is related to the Oligocene rifting of the URG and its subsequent exposure to the Alpine push: as evidenced by the formation of subbasins individualized by transverse ENE–WSW thresholds, ENE–WSW structures acted as transfer zones to accommodate the *N–S* Eocene compression and the *E–W* Oligocene extension forming the submeridian normal faults (Villemin & Bergerat 1987; Brun *et al*. 1992; Chorowicz & Deffontaines 1993; Schumacher 2002; Michon & Sokoutis 2005). On the contrary, Edel *et al.* (2007) argue that the wrenching and then transtension occurring on NE–SW faults in the same periods constitute the main reactivation processes controlling the formation of the URG. Whatever the contribution of each population, NE–SW, ENE–WSW and NW–SE structures experienced strike-slip movements from Eocene to Actual as shown by striated planes in the Rhine Graben (Villemin & Bergerat 1987; Genter 1990; Lopes Cardozo & Behrmann 2006) and in the Soultz-sous-Forêts basement (Dezayes 1995). Significant vertical movements occurred mainly along ∼N–S to NE–SW normal faults, forming tilted blocks.

Within the Soultz-sous-Forêts basement, the N–S mean azimuth of fractures measured by borehole imaging and the thickest veins exhibiting N–S trend have been interpreted as the signatures of the Oligocene extension (Genter & Traineau 1996; Dezayes *et al*. 2010). The VSP reflectors trending ∼N026°E and ∼N167°E could be related to these deformations as well. However, the volume in which all these structures occur is located within the Soultz-sous-Forêts Horst (Cautru 1989; Renard & Courrioux 1994; Sausse *et al*. 2010). Only minor vertical offsets of the top of basement are observed (Place *et al*. 2010, see right part of Fig. 1b). Thus, the faults recognized within the basement cannot have accommodated large vertical movements. Mode I dominated opening of fractures can be envisaged, as well as strike-slip movements that could explain a flower-like structure expressed at the basis of the sedimentary cover east of the Soultz-sous-Forêts fault (Fig. 1b).

The Miocene to Actual NW–SE Alpine push results in strike-slip movements along N–S faults in the URG, and transpressional movement along NNE–SSW structures (Lopes Cardozo & Behrmann 2006; Rotstein & Schaming 2008). In the Soultz-sous-Forêts EGS, the maximal horizontal principal stress is oriented ∼N170°E ± 15° (Cornet *et al*. 2007; Valley 2007). In such conditions, the major fault GPK3-FZ4770 oriented N150°E would act as a right-lateral strike-slip fault. If the reflectors PS3-int-seg and PS3-low-seg are supposed to be continuous prior to this Neogene strike-slip deformation, their right-lateral offset value attaining ∼100 m supports such expected movement along the GPK3-FZ4770 fault (Fig. 8).

Microseismicity and drilling-induced tension fractures indicate that the maximal principal stress is almost horizontal at depth in the basement (Cuenot *et al.* 2006; Valley 2007; Dorbath *et al.* 2010). It becomes vertical in the upper part of the basement where the VSP reflectors are identified, the transition zone being located at about 3600–5000 m. In such conditions, the difference between the value of the vertical stress and the maximal horizontal stress is quite low (Evans 2005). Fault throws showing both normal and strike-slip components are thus expected. The dip values of the planes investigated by VSP range between 51° and 68° (Table 1), that could reflect partially normal movements. The ENE–WSW orientation of the minimum horizontal stress (Cuenot *et al*. 2006; Valley 2007; Dorbath *et al*. 2010) is in favour of normal slip along submeridian structures. But such major structures lack within the tilted blocks and the Soultz-sous-Forêts Horst (Fig. 1b). Some planes ∼N167°E are activated, but other orientations are significantly recognized as well around the N026°E, N057°E and N120°E directions (Fig. 9). Thus, they probably represent the thickest and more mature structures occurring within the reservoir, due to their major role in the Variscan period and their further development by reactivations during the Tertiary episodes reported earlier (Eocene compression, Oligocene extension and subsequent strike-slip regimes, (Villemin & Bergerat 1987; Schumacher 2002; Édel *et al.* 2007)) and currently activated in a very likely strike-slip regime. In the URG, the neotectonic activity of faults trending NE–SW, ENE–WSW and NW–SE is incidentally observed (Chorowicz & Deffontaines 1993; Lemeille *et al*. 1999). All these orientations, as well as submeridian directions corresponding to Oligocene normal faulting, are recognized in the Soultz-sous-Forêts area by the analysis of satellite pictures, suggesting recent activity (Genter 1990; Valley 2007).

The average dip value of the VSP reflectors is approx. 60° (Table 1). This value is too high to reflect Variscan thrusts and ramps. Nevertheless, it could be associated to suture zones located to the South (Vittel-Baden-Baden fault zone) or to the North (Tepla suture, Fig. 1) that can exhibit highly dipping structures (Édel & Schulmann 2009). Their orientation is also suitable to locate the Tertiary strike-slip movements described earlier.

The particular seismic behaviour of the faults (*P–S* reflection) is linked to their inner properties, which have to be discussed.

The VSP data presented here were acquired in May 1993 prior to any stimulation of the acquisition depth intervals. The clearest *P–S* arrivals intersecting the *P* direct wave correspond to the faults encountered at 2860 and 3490 m in GPK1. These faults are responsible for the major natural flow anomalies of the open hole section (e.g. Evans *et al.* 2005a). Less clear arrivals of *P–S* or *P–P* mode (GPK1–2960, GPK1–3090, GPK1–3325, EPS1–2070 and EPS1–2160) seem to be associated with fracture zones of weaker permeability (Genter *et al.* 1995; Evans *et al.* 2005a; Sausse & Genter 2005; Sausse *et al.* 2006). Within the 2850–3400 m depth interval in GPK1, structures intersected around 2860, 2960 and 3090 m have shown displacement after stimulation by massive water injection (Cornet *et al*. 1997; Evans *et al.* 2005a). Some of these low-permeability zones are highly fractured and altered, and secondary precipitations are found. Other altered and fractured levels are observed without flow anomaly (Sausse *et al*. 2006). These observations indicate past fluid circulations and the present day closure of the connected porosity within the faults. In some cases, the present day filling-up of the fault might be local (at the borehole location) and permeability could perhaps be preserved away from the borehole (far-reaching in the whole fault). Only one structure responsible for flow anomaly and tectonic dislocation located at about 3220 m in GPK1 (Cornet *et al.* 1997; Sausse & Genter 2005) is not detected on the processed VSP data (Fig. 4).

According to the VSP results and borehole data (see references cited earlier), the faults intersected at 2860 m (PS1), 3490 m (PS2) in GPK1 and at 3514 m (PS3-int-seg) in GPK2 are major faults. They locate major fluid circulations (Tenzer *et al.* 1999; Aquilina

et al. 2004; Sausse & Genter 2005). The reflector producing the arrival PS3-upp-seg could be of similar importance. The mean horizontal spacing of these faults is about 450 m (Fig. 8). This system is considered to be cut by the large fault GPK3-FZ4770 m presenting 3000 m of extension from its intersection with GPK3 and the reflector PS6 (Sausse *et al*. (2010), and this study). 3-D fluid flow modelling shows that a mainly ∼N–S trending fracture population cannot explain the observed hydraulic behaviour of the reservoir (Gentier *et al.* 2010). NE–SW and NW–SE striking sets play an important role in fluid transfers. VSP and modelling results are thus in agreement.

To summarize, the strongest VSP reflections (PS1, PS2, PS3 and PS6) correspond to the highest flow anomalies—if intersected by the well—, or to the structures that seem to have the greatest extents (GPK3-FZ4770) (Fig. 8). These results show that major flow anomalies and interwell hydraulic connections are concentrated by these main faults occurring with a spacing of some hundreds of metres. These faults form structural blocks with flowing borders. Inside these blocks, the structures (GPK1–2960, GPK1–3090, GPK1–3325, EPS1–2070 and EPS1–2160) seem to make a less important contribution to fluid transfer (Genter *et al.* 1995; Sausse *et al.* 2006). Thus, a good correlation is observed between the *P–S* reflectivity of a fault and its potential hydraulic and tectonic activity. The elastic response of a fault seems to be strongly related to its porosity network and fluid conditions, that could imply in some cases a mechanical defect (Schoenberg 1980; Jones & Nur 1984; Lüschen *et al.* 1993; Carr *et al.* 1996; Harjes *et al.* 1997; Harjes *et al.* 1998; Smithson *et al.* 2000; Rabbel *et al.* 2004), although this phenomenon has never been satisfactorily explained by theoretical work. In addition to the fluid content, the anisotropy induced by the fractures in the damage zones of the faults could be of importance in the reflection coefficients (see among others Zillmer *et al.* 1997). Some computations have been carried out by Behura & Tsvankin (2006) and Cai & Chen (2009) showing in a simple case study that the *P–S* reflection coefficient may attain a value of ∼0.065 for a incidence value of 60°. Nevertheless, no value is computed regarding the *P–P* reflection coefficient. Thus, it cannot be compared to those from *P–S*, that could, however, help explaining the surprising absence of *P–P* reflection in the present data set.

VSP and microseismic results provide structural data at the reservoir scale. They represent valuable data to resolve some hydraulic relationships between the boreholes evidenced by tracer tests (Sausse *et al.* (2010) and this paper). Our study benefited from microseismic clouds to attribute some reflections (PS2-upp-seg and PS6) to the GPK3-FZ4770 with confidence. However, seismic activity is undesirable regarding public acceptance (Gérard *et al*. 2006; Petty *et al.* 2009). Thus, a VSP survey carried out with several acquisition boreholes and a larger number of sources than in 1993 may represent a reliable way to investigate a fractured reservoir with controlled and very low environmental risks.

8 CONCLUSION

A full sequence of processing, analysing and interpreting VSP data recorded in a granitic basement is illustrated, where conventional seismic reflection has not imaged any structure. High-quality 3C data presenting a high signal/noise ratio obtained after isotropic processing allow clear *P–S* reflections to be identified. Reflections are found to occur on faults developed at the reservoir scale showing flow anomalies at well intersections. Their 3-D mapping in the existing reservoir model allowed some useful comparisons with other data, especially microseismic clouds providing also some structural information at the same scale range. This shows that the basement is cut in several hectometer-scale blocks by faults. Major flow paths occur within these faults very probably inherited from Variscan and Tertiary times reactivated due to the maximal stress oriented vertically in the studied area. The structural results are in accordance with previous studies of the hydraulic behaviour of the fractures intersected in GPK1 and EPS1. In particular, the good hydraulic connections between GPK1, GPK2 and GPK3 are explained by the occurrence of a fault extending over 4 km (GPK3-FZ4770), although this structure is weakly expressed in the sedimentary cover.

ACKNOWLEDGMENTS

The authors acknowledge the European Economic Interest Group 'GEIE Exploitation Minière de la Chaleur' (Kutzenhausen, France), which was supported mainly by the European Commission, BMU (Germany), ADEME (France) and by a consortium of industrial members (EDF, EnBW, ES, Pfalzwerke, Evonik). J. Place benefited from a PhD grant supported by ADEME and EIfER. Thanks also to the reviewers, Michael Worthington and one anonymous, for their comments on the manuscript and further constructive discussions. Gordon Filby is acknowledged for improvement of the English style. François Henry Cornet and Marc Schaming (Université de Strasbourg, France) are thanked for providing and successfully reading the old VSP data. Data processing was applied by Martin Cox (VSfusion, London, UK) to whom we are also grateful. André Gérard and Albert Genter (respectively former and current GEIE scientific supervisors) are acknowledged for their continued support.

REFERENCES

Al-Ali, Z.A., *et al.*, 2009. Looking deep into the reservoir, *Oilfield Rev.,* **21**(2), 38–47.

Aquilina, L. & Brach, M., 1995. Characterization of Soultz hydrochemical system: WELCOM (Well Chemical On-line Monitoring) applied to deepening of GPK-1 borehole, *Geotherm. Sci. Technol.,* **4**(4), 239–251.

Aquilina, L., De Dreuzy, J.-R., Bour, O. & Davy, P., 2004. Porosity and fluid velocities in the upper continental crust (2 to 4 km) inferred from injection tests at the Soultz-sous-Forêts geothermal site, *Geochim. cosmochim. Acta.,* **68**(11), 2405–2415.

Arthaud, F. & Matte, P., 1975. Les décrochements tardi-hercyniens du sud-ouest de l'Europe. Géométrie et essai de reconstitution des conditions de la déformation, *Tectonophysics,* **25,** 139–171.

Beauce, A., Fabriol, H., Le Masne, D., Cavoit, C., Mechler, P. & Chen, X.K., 1991. Seismic studies on the HDR site of Soultz-sous-Forets (Alsace, France), *Geotherm. Sci. Technol.,* **3,** 239–266.

Behura, J. & Tsvankin, I., 2006. Small-angle AVO response of PS-waves in tilted transversely isotropic media, *Geophysics,* **71**(5), C69–C79.

Bourgeois, O., Ford, M., Diraison, M., Le Carlier de Veslud, C., Gerbault, M., Pik, R., Ruby, N. & Bonnet, S., 2007. Separation of rifting and lithospheric folding signatures in the NW-Alpine foreland, *Int. J. Earth Sci.,* **96,** 1003–1031.

Bourouis, S. & Bernard, P., 2007. Evidence for coupled seismic and aseismic fault slip during water injection in the geothermal site of Soultz (France), and implications for seismogenic transients, *Geophys. J. Int.,* **169**(2), 723–732.

Brun, J.P., Gutscher, M.A. & the DEKORP-ECORS team, 1992. Deep crustal structure of the Rhine graben from DEKORP-ECORS seismic reflexion data: a summary, *Tectonophysics,* **208,** 139–147.

Cai, X.G. & Chen, X.F., 2009. Study on the reflection-transmission coefficients of elastic waves in the media with dipping fractures, *Chin. J. Geophys. (Acta Geophys. Sin.),* **52**(5), 1253–1262.

Carr, B.J. *et al*., 1996. Vertical seismic profile results from the Kola Superdeep Borehole, Russia, *Tectonophysics,* **264**(1–4), 295–307.

Cautru, J.P., 1989. Coupe géologique passant par le forage GPK1 calée sur la sismique réflexion, et documents annexes. IMRG, EEIG "Heat Mining" Internal Report, Kutzenhausen, France.

Charléty, J., Cuenot, N., Dorbath, C. & Dorbath, L., 2006. Tomographic study of the seismic velocity at the Soultz-sous-Forêts EGS/HDR site, *Geothermics,* **35**(5–6), 532–543.

Childs, C., Manzocchi, T., Walsh, J.J., Bonson, C.G., Nicol, A. & Schöpfer, M.P.J., 2009. A geometric model of fault zone and fault rock thickness variations, *J. Struct. Geol*., **31**(2), 117–127.

Chorowicz, J. & Deffontaines, B., 1993. Transfer faults and pull-apart model in the Rhinegraben from analysis of multisource data, *J. geophys. Res.,* **98**(B8), 14339–14351.

Cocherie, A., Guerrot, C., Fanning, C.M. & Genter, A., 2004. Datation U-Pb des deux faciès du granite de Soultz (Fossé rhénan, France), *Comptes Rendus Geosciences,* **336**(9), 775–787.

Cornet, F.H., Helm, A., Poitrenaud, H. & Etchecopar, A., 1997. Seismic and aseismic slips induced by large-scale fluid injections, *Pure appl. Geophys.,* **150,** 563–583.

Cornet, F.H., Bérard, T. & Bourouis, S., 2007. How close to failure is a granite rock mass at a 5 km depth?, *Int. J. Rock Mech. Min. Sci.,* **44,** 47–66.

Cosma, C., Heikkinen, P., Keskinen, J. & Enescu, N., 2001. VSP in crystalline rocks-from downhole velocity profiling to 3-D fracture mapping, *Int. J. Rock Mech. Min. Sci.,* **38,** 843–850.

Cuenot, N., Charléty, J., Dorbath, L. & Haessler, H., 2006. Faulting mechanisms and stress regime at the European HDR site of Soultz-sous-Forêts, France, *Geothermics,* **35**(5–6), 561–575.

Cuenot, N., Dorbath, C. & Dorbath, L., 2008. Analysis of the microseismicity induced by fluid injections at the EGS site of Soultz-sous-Forêts (Alsace, France): implications for the characterization of the geothermal reservoir properties, *Pure appl. Geophys.*, **165**(5), 797–828.

Dezayes, C., 1995. Caractérisation et interprétation d'un volume rocheux fracturé à partir de données de forages. Les forages géothermiques de Soultz-sous-Forêts et autres exemples d'échantillonnages unidirectionnels, *PhD thesis*, Université de Savoie, Chambéry, pp. 246.

Dezayes, C., Genter, A. & Valley, B., 2010. Structure of the low permeable naturally fractured geothermal reservoir at Soultz, *Comptes Rendus Geoscience,* **342**(7–8), 517–530.

Dèzes, P., Schmid, S.M. & Ziegler, P.A., 2004. Evolution of the European Cenozoic Rift System: interaction of the Alpine and Pyrenean orogens with their foreland lithosphere, *Tectonophysics,* **389**(1–2), 1–33.

Dorbath, L., Cuenot, N., Genter, A. & Frogneux, M., 2009. Seismic response of the fractured and faulted granite of Soultz-sous-Forêts (France) to 5 km deep massive water injections, *Geophys. J. Int.,* **177**(2), 653–675.

Dorbath, L., Evans, K., Cuenot, N., Valley, B., Charléty, J. & Frogneux, M., 2010. The stress field at Soultz-sous-Forêts from focal mechanisms of induced seismic events: cases of the wells GPK2 and GPK3, *Comptes Rendus Geoscience,* **342**(7–8), 600–606.

Dylikowski, J., 1985. Etude en stratigraphie sismique de remplissage tertiaire de la région de Péchelbronn (Fossé Rhénan). Application au développement pétrolier en domaine de fossé d'effondrement. *PhD thesis*, Université de Paris Orsay.

Édel, J.B. & Schulmann, K., 2009. Geophysical constraints and model of the "Saxothuringian and Rhenohercynian subductions – magmatic arc system" in NE France and SW Germany, *Bull. Soc. Géol. France,* **180**(6), 545–558.

Édel, J.B., Schulmann, K. & Rotstein, Y., 2007. The Variscan tectonic inheritance of the Upper Rhine Graben: evidence of reactivations in the Lias, Late Eocene–Oligocene up to the recent, *Int. J. Earth Sci.,* **96**(2), 305–325.

Eisbacher, G.H., Luschen, E. & Wickert, F., 1989. Crustal-scale thrusting and extension in the Hercynian Schwarzwald and Vosges, Central Europe, *Tectonics,* **8**(1), 1–21.

Emsley, S.J., Shiner, P., Enescu, N., Beccacini, A. & Cosma, C., 2007. Using VSP surveys to bridge the scale gap between well and seismic data, *Geol. Soc. Lond. Spec. Publ.,* **270**(1), 83–91.

Evans, K.F., 2005. Permeability creation and damage due to massive fluid injections into granite at 3.5 km at Soultz: 2. Critical stress and fracture strength, *J. geophys. Res.,* **110,** B04204, doi:10.1029/2004JB003169.

Evans, K.F., Genter, A. & Sausse, J., 2005a. Permeability creation and damage due to massive fluid injections into granite at 3.5 km at Soultz: 1. Borehole observations, *J. geophys. Res.,* **110,** B04203, doi:10.1029/2004JB003168.

Evans, K.F. *et al*., 2005b. Microseismicity and permeability enhancement of hydrogeologic structures during massive fluid injections into granite at 3 km depth at the Soultz HDR site, *Geophys. J. Int.,* **160**(1), 388–412.

Franke, W., 2006. The Variscan orogen in Central Europe: construction and collapse, *Geol. Soc. Lond. Memoirs,* **32,** 333–343.

Gaucher, E., 1998. Comportement hydromécanique d'un massif fracturé: apport de la microsismicité induite. Application au site géothermique de Soultz-sous-Forêts, *PhD thesis*. Institut de Physique du Globe, Paris, p. 245.

Genter, A., 1990. Géothermie roches chaudes sèches. Le granite de Soultz-sous-Forêts (Bas-Rhin, France). Fracturation naturelle, altérations hydrothermales et interaction eau-roche, *PhD thesis*, Université d'Orléans, Orléans, p. 201.

Genter, A., 1993. Géométrie des zones fracturées et hydrothermalisées dans le granite de Soultz-sous-Forêts (forages GPK-1 et EPS-1), BRGM Technical Internal Note N°RCS93T99, 15 July 1993.

Genter, A. & Traineau, H., 1996. Analysis of macroscopic fractures in granite in the HDR geothermal well EPS-1, Soultz-sous-Forets, France, *J. Volc. Geotherm. Res.,* **72**(1–2), 121–141.

Genter, A., Traineau, H., Dezayes, C., Elsass, P., Ledesert, B., Meunier, A. & Villemin, T., 1995. Fracture analysis and reservoir characterization of the granitic basement in the HDR Soultz project (France), *Geotherm. Sci. Technol.,* **4**(3), 189–214.

Genter, A., Castaing, C., Dezayes, C., Tenzer, H., Traineau, H. & Villemin, T., 1997. Comparative analysis of direct (core) and indirect (borehole imaging tools) collection of fracture data in the Hot Dry Rock Soultz reservoir (France), *J. geophys. Res.,* **102**(B7), 15 419–15 431.

Genter, A., Evans, K., Cuenot, N., Fritsch, D. & Sanjuan, B., 2010. Contribution of the exploration of deep crystalline fractured reservoir of Soultz to the knowledge of enhanced geothermal systems (EGS), *Comptes Rendus Geoscience,* **342**(7–8), 502–516.

Gentier, S. *et al*., 2002. Modélisation de l'interface puits-échangeur (site de Soultz-sous-Forêts). Acquisition de données de base et développements préliminaires, Report BRGM/RP 51764-FR.

Gentier, S., Rachez, X., Tran Ngoc, T.D., Peter-Borie, M. & Souque, C., 2010. 3D flow modelling of the medium-term circulation test performed in the deep geothermal site of Soultz-sous-Forêts (France) World Geothermal Congress, 2010 April 25–30, Bali, Indonesia, p. 11.

Gérard, A. & Kappelmeyer, O., 1987. The Soultz-sous-Forets project, *Geothermics,* **16**(4), 393–399.

Gérard, A., Menjoz, A. & Schwoerer, P., 1984. L'anomalie thermique de Soultz-sous-Forêts, *Géothermie Actualités,* **3,** 35–42.

Gérard, A., Cuenot, N., Charléty, J., Dorbath, C., Dorbath, L., Gentier, S. & Haessler, H., 2006. Elements governing the ratio (Hydraulic performance)/(induced microseismic nuisances) during the stimulation of "EGS Soultz Type" reservoirs, Paper of EHDRA Scientific Conference 2006 June, Soultz-sous-Forêts, France, p. 6.

Green, A.G. & Mair, J.A., 1983. Subhorizontal fractures in a granitic pluton: their detection and implications for radioactive waste disposal, *Geophysics,* **48**, 1428–1449.

Harjes, H.P. *et al*., 1997. Origin and nature of crystal reflections: Results from integrated seismic measurements at the KTB superdeep drilling site, *J. geophys. Res.,* **102**(B8), 18 267–18 288.

Harjes, H.P., Janik, M., Müller, J. & Bliznetsov, M., 1998. Imaging of crustal structures from vertical array measurements, *Tectonophysics,* **286**(1–4), 185–192.

Hesthammer, J. & Fossen, H., 2003. From seismic data to core data: an integrated approach to enhance reservoir characterization, *Geol. Soc. Lond. Spec. Publ.,* **209**(1), 39–54.

Jones, R.H., 1993. Active seismic surveys at the Soultz site, Paper of EHDRA Scientific Conference, 1993 May, Soultz-sous-Forêts, France, p. 4.

Jones, T.D. & Nur, A., 1984. The nature of seismic reflections from deep crustal fault zones, *J. geophys. Res.,* **89**(B5), 3153–3171.

Juhlin, C., 1995. Imaging of fracture zones in the Finnsjön area, central Sweden, using the seismic reflection method, *Geophysics,* **60**(1), 66–75.

Juhlin, C., Dehghannejad, M., Lund, B., Malehmir, A. & Pratt, G., 2010. Reflection seismic imaging of the end-glacial Pärvie Fault system, northern Sweden, *J. appl. Geophys.,* **70**(4), 307–316.

Jung, R., Reich, W., Engelking, U., Hettkamp, T. & Weidler, R., 1995. Hydraulic tests in 1995 at the HDR Project, Soultz-sous-Fôrets, France. Field Report, Bundesanstalt für Geowissenschaften und Rohstoffe (BGR), Hannover, Germany.

Jupe, A., Jones, R.J., Willis-Richards, J., Dyer, B., Nicholls, J. & Jacques, P., 1994. Report on HDR phase 4 – Activity 4.1 Soultz experimental programme 1993/1994, CSM Associates Limited.

Kohl, T., Baujard, C. & Mégel, T., 2006. Conditions for mechanical re-stimulation of GPK4. Paper of EHDRA Scientific Conference, 2006 June, Soultz-sous-Forêts, France, p. 6.

Le Bégat, S., Cornet, F.H. & Farra, V., 1994. Etude de la percolation de fluides par sismique active sur le site de Soultz-sous-Forêts. ADEME Report (Agence pour la Défense de l'Environnement et la Maîtrise de l'Energie).

Lemeille, F., Cushing, M.E., Cotton, F., Grellet, B., Ménillet, F., Audru, J.-C., Renardy, F. & Fléhoc, C., 1999. Traces d'activité pléistocène de failles dans le Nord du fossé du Rhin supérieur (plaine d'Alsace, France), *Comptes Rendus de l'Académie des Sciences – Series IIA – Earth and Planetary Science,* **328**(12), 839–846.

Lopes Cardozo, G.G.O. & Behrmann, J.H., 2006. Kinematic analysis of the upper Rhine graben boundary fault system, *J. Struct. Geol.,* **28**(6), 1028–1039.

Lüschen, E., Sobolev, S., Werner, U., Söllner, W., Fuchs, K., Gurevich, B. & Hubral, P., 1993. Fluid reservoir (?) beneath the KTB drillbit indicated by seismic shear-wave observations, *Geophys. Res. Lett.,* **20**(10), 923–926.

Luthi, S.M., 2005. Fractured reservoir analysis using modern geophysical well techniques: application to basement reservoirs in Vietnam, *Geol. Soc. Lond. Spec. Publ*., **240**(1), 95–106.

Macé, L., 2006. Caractérisation et modélisation numériques tridimensionnelles de réservoirs naturellement fracturés, *PhD thesis*, Institut National Polytechnique de Lorraine, Nancy, p. 152.

Macé, L., Souche, L. & Mallet, J.L., 2004. 3D fracture modeling integrating geomechanics and geologic data, in *Proceedings of the AAPG International Conference,* October 24–27, Cancun, Mexico.

Mallet, J.L., 2002. *Geomodeling*, Oxford University Press, New York, NY, p. 624.

Mari, J.L., Coppens, F. & Revol, J., 2003. *Well Seismic Surveying*, Editions Technip, Paris, France, p. 238.

Martí, D., Escuder Viruete, J., Carbonell, R., Flecha, I. & Pérez-Estaún, A., 2006. Fault architecture and related distribution of physical properties in granitic massifs: geological and geophysical methodologies, *J. Iberian Geol.,* **32**(1), 95–112.

Miao, X.-G., Moon, W.M. & Milkereit, B., 1995. A multioffset, three-component VSP study in the Sudbury Basin, *Geophysics,* **60**(2), 341–353.

Michon, L. & Sokoutis, D., 2005. Interaction between structural inheritance and extension direction during graben and depocentre formation: an experimental approach, *Tectonophysics,* **409**(1–4), 125–146.

Milkereit, B., Green, A., Wu, J., White, D. & Adam, E., 1994. Integrated seismic and borehole geophysical study of the Sudbury Igneous Complex, *Geophys. Res. Lett.,* **21**(10), 931–934.

Newman, G.A., Gasperikova, E., Hoversten, G.M. & Wannamaker, P.E., 2008. Three-dimensional magnetotelluric characterization of the Coso geothermal field, *Geothermics,* **37,** 369–399.

Petty, S., Livesay, B., Clyne, M. & Baria, R., 2009. Bringing down the cost of EGS power, *Geotherm. Res. Council, Transact.,* **33,** 229–233.

Place, J., Diraison, M., Naville, C., Géraud, Y., Schaming, M. & Dezayes, C., 2010. Decoupling of deformation in the Upper Rhine Graben sediments. Seismic reflection and diffraction on 3-component Vertical Seismic Profiling (Soultz-sous-Forêts area), *Comptes Rendus Geoscience,* **342**(7–8), 575–586.

Rabbel, W. *et al*., 2004. Superdeep vertical seismic profiling at the KTB deep drill hole (Germany): seismic close-up view of a major thrust zone down to 8.5 km depth, *J. geophys. Res.,* **109**(B9), B09309, doi:10.1029/2004JB002975.

Renard, P. & Courrioux, G., 1994. Three-dimensional geometric modelling of a faulted domain: the Soultz horst example (Alsace, France), *Comput. Geosci*., **20**(9), 1379–1390.

Rotstein, Y. & Schaming, M., 2008. Tectonic implications of faulting styles along a rift margin: the boundary between the Rhine Graben and the Vosges Mountains, *Tectonics,* **27**(2), TC2001, doi:10.1029/2007TC002149.

Sausse, J. & Genter, A., 2005. Types of permeable fractures in granite, *Geol. Soc. Lond. Spec. Publ.,* **240**(1), 1–14.

Sausse, J., Fourar, M. & Genter, A., 2006. Permeability and alteration within the Soultz granite inferred from geophysical and flow log analysis, *Geothermics,* **35**(5–6), 544–560.

Sausse, J., Dezayes, C., Dorbath, L., Genter, A. & Place, J., 2010. 3D model of fracture zones at Soultz-sous-Forêts based on geological data, image logs, induced microseismicity and vertical seismic profiles, *Comptes Rendus Geoscience,* **342**(7–8), 531–545.

Schoenberg, M., 1980. Elastic wave behaviour across linear slip interfaces, *J. acoust. Soc. Am.,* **68**(5), 1516–1521.

Schumacher, M.E., 2002. Upper Rhine Graben: role of preexisting structures during rift evolution, *Tectonics,* **21**(1), 17, doi:10.1029/2001TC900022.

Schutter, S.R., 2003. Hydrocarbon occurrence and exploration in and around igneous rocks, *Geol. Soc. Lond. Spec. Publ.,* **214**(1), 7–33.

Sittler, C., 1985. Les hydrocarbures d'Alsace dans le contexte historique et géodynamique du fossé Rhénan, *Bulletin des Centres de Recherches Elf Exploration Production,* **9**(2), 335–371.

Smithson, S.B., Wenzel, F., Ganchin, Y.V. & Morozov, I.B., 2000. Seismic results at Kola and KTB deep scientific boreholes: velocities, reflections, fluids, and crustal composition, *Tectonophysics,* **329**(1–4), 301–317.

Spencer, C., Thurlow, G., Wright, J., White, D., Carroll, P., Milkereit, B. & Reed, L., 1993. A vibroseis reflection seismic survey at the Buchans Mine in central Newfoundland, *Geophysics,* **58**(1), 154–166.

Tenzer, H., Schanz, U. & Homeier, G., 1999. Development and characterisation of a HDR heat exchanger at the HDR test site at Soultz-sous-Forêts: Flow logs, joint systems and hydraulic active fractures, in *Proceedings of European Geothermal Conference,* Basel, September 28–30, **2,** 99–107.

Tirén, S.A., Askling, P. & Wänstedt, S., 1999. Geologic site characterization for deep nuclear waste disposal in fractured rock based on 3D data visualization, *Eng. Geol.,* **52,** 319–346.

Valley, B., 2007. The relation between natural fracturing and stress heterogeneities in deep-seated crystalline rocks at Soultz-sous-Forêts (France), *PhD thesis*, Eidgenössische Technische Hochschule, Zurich, p. 297.

Villemin, T. & Bergerat, F., 1987. L'évolution structurale du fossé Rhénan au cours du Cénozoique: un bilan de la déformation et des effets thermiques de l'extension, *Bull. Soc. Géol. France,* **3,** 245–256.

Weidler, R., Gérard, A., Baria, R., Baumgaertner, J. & Jung, R., 2002. Hydraulic and micro-seismic results of a massive stimulation test at 5 km depth at the European Hot-Dry-Rock test site Soultz, France, Twenty-Seventh Workshop on Geothermal Reservoir Engineering, Stanford University, CA, pp. 95–100.

Ziegler, P.A., 1986. Geodynamic model for the Palaeozoic crustal consolidation of Western and Central Europe, *Tectonophysics,* **126**(2–4), 303–328.

Ziegler, P.A., 1992. European Cenozoic rift system, *Tectonophysics,* **208**(1–3), 91–111.

Ziegler, P.A., Schumacher, M.E., Dèzes, P., Van Wees, J.-D. & Cloetingh, S., 2006. Post-Variscan evolution of the lithosphere in the area of the European Cenozoic Rift System, *Geol. Soc. Lond. Memoirs,* **32,** 97–112.

Zillmer, M., Gajewski, D. & Kashtan, B.M., 1997. Reflection coefficients for weak anisotropic media, *Geophys. J. Int.,* **129**(2), 389–398.

APPENDIX

Some seismic arrivals recorded on Fig. 4 do not occur on the whole data set or do not seem to be *P–S* arrivals. This section is devoted to their specific interpretation and to the characterization of the uncertainties regarding the modelling results. See Section 5.3 for the significance of $*$.

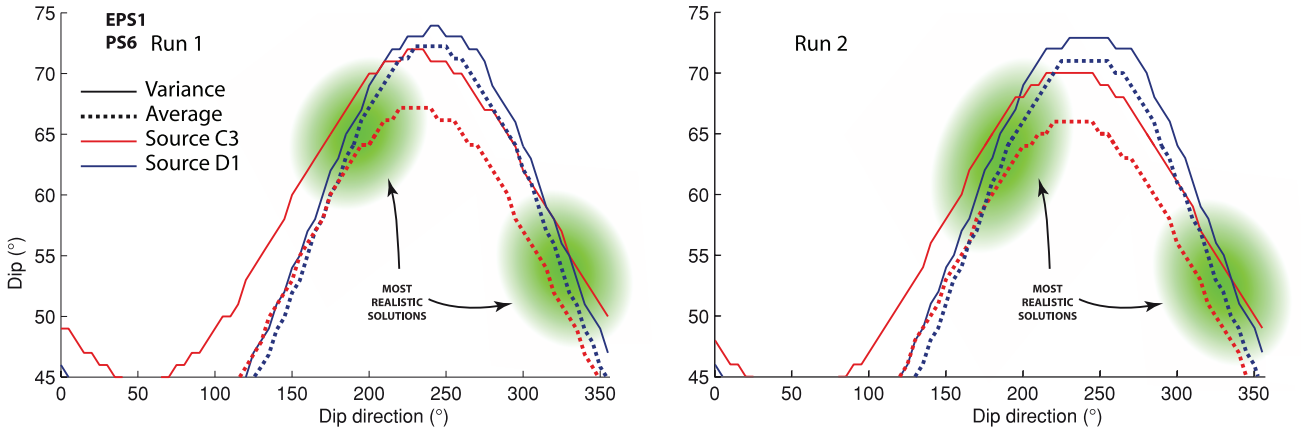

Figure A1. Arrival EPS1–PS6: variance and average of the residuals (difference between modelled and observed traveltimes) in function of the orientation of the modelled reflector.

PS1**

Its time–depth curve is linear on all the records except on offset A3 run 1 where it looks hyperbolic (Fig. 4). Only the run 2 has been used.

PS2 (lower and upper segments***)

Modelling is very efficient in reproducing the observed traveltimes. This allows us to be very confident in the results (Fig. 7), even if the number of traces is restricted regarding the PS2-lower segment (Fig. 4).

PS3 (* or **)

The traveltimes observed from source B are systematically in disagreement with the modelled traveltimes. Several slightly different time picking data sets were no more successful. Thus, the data from source B are not taken into account, and results are produced from three sources only.

General comments on PS4 (**), PS5 (*) and PS6 (*)

Only three profiles acquired from two source positions are available in the EPS1 well (Fig. 4), thus the results have to be considered with caution.

PS4 (**)

Even if the modelled traveltimes satisfactorily match the observations, caution is necessary because of the restricted number of sources provoking this reflection.

PS5 (*)

Results from average and variance of the residuals do not show a coherency as clear as concerning the other arrivals.

PS6 (*)

Although a large number of clear traces is available (Fig. 4), the orientation implying the lowest residual is not well defined. As shown in Fig. A1, the minimum curves are close enough to each other so that their intersections are unclear and not single. Two orientations represented by green zones in Fig. A1 roughly reproduce the observed time–depth curves.

EPS1–2160

This arrival appears only on the horizontal north component of the VSP shot from D1 (Fig. 4). Three possibilities have to be considered to produce a signal only on horizontal components (Fig. A2): (i) a *P* wave reflected by a moderately dipping interface may propagate horizontally (Fig. A2a), (ii) a direct downgoing *S* wave produced by a source close to a zero offset position (Fig. A2b) and (iii) an *S* wave reflected by a subhorizontal interface (Fig. A2c). The event EPS1–2160 arrives too early and presents a negative apparent velocity that is rejected in the case of Fig. A2b. A *P*–*P* reflection on a dipping structure (Fig. A2a) would present a time–depth curve close to the *P* direct arrival, which is not observed. On the one hand, the event EPS1–2160 is partially blended with the *P* direct arrival, and on the other hand the absolute value of its apparent velocity is lower that the velocity of the direct *P* wave. Only a *P*–*S* reflection on a subhorizontal reflector could explain both the polarity and the time–depth curve of the arrival EPS1–2160 (Fig. A2c).

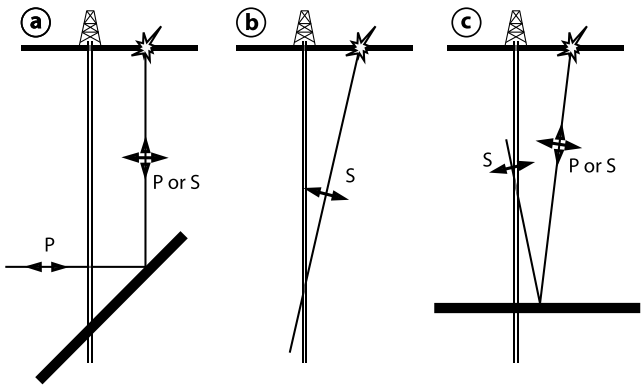

Figure A2. Three travelpaths and polarisations explaining a horizontal polarization recorded on 3C VSP data. (a) *P*-wave travelling almost horizontally after a reflection on a dipping interface. (b) *S* direct wave travelling almost vertically. (c) *S*-wave travelling almost vertically after a reflection on a horizontal interface.

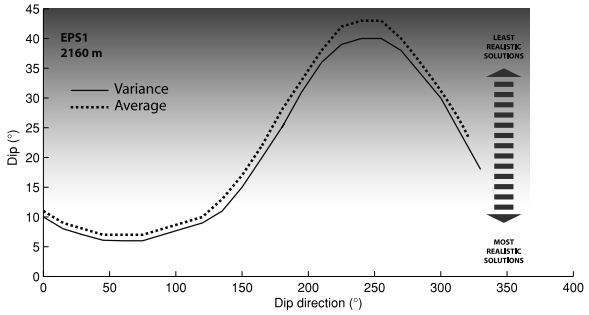

Figure A3. Arrival EPS1–2160: variance and average of the residuals (difference between modelled and observed traveltimes) in function of the orientation of the modelled reflector.

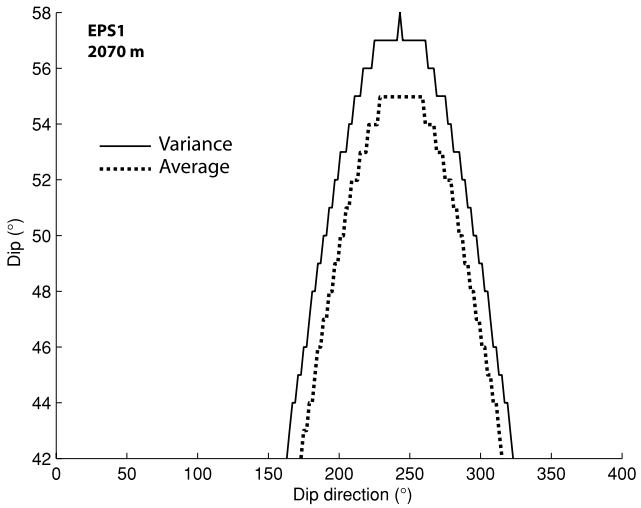

Figure A4. Arrival EPS1–2070: variance and average of the residuals (difference between modelled and observed traveltimes) in function of the orientation of the modelled reflector.

Modelling is not able to provide definite values of dip and dip directions because the event is observed on only one VSP. The result is a domain of possible orientations (Fig. A3); values of dip direction between 330° and 150° are inferred for a gently dipping reflector. The N–S polarization of the wave (Fig. 4) is not sufficiently reliable to derive the strike of the reflector, as the understanding of elastic processes occurring in a *P*–*S* reflection at almost normal incidence is incomplete. Fracture surveying provided different results regarding the orientation of the fracture (N278°E 53° and N285°E 37°, respectively after Dezayes *et al*. 2010 and Genter *et al*. 1995). The latter value is in accordance with the results derived by VSP, both in azimuth and dip. Nevertheless, this does not mean that the structure detected by VSP and the structure imaged at the borehole wall scale are the exactly the same.

EPS1–2070

Only the vertical component of VSP acquired from D1 exhibits an event at 2070 m in EPS1 (Fig. 4). Such a signal may be generated either by a *P* wave reflected by a horizontal interface, either by a *P*–*S* conversion on a dipping reflector (Fig. 5). The time–depth curve of the event is not a 'mirror' of the *P* direct wave, thus the absolute apparent velocity values of the two events are different. The only case that has to be considered is the *P*–*S* reflection. As a consequence, the minimum curves of average and variance produced by modelling have to be considered for high dip values (Fig. A4).

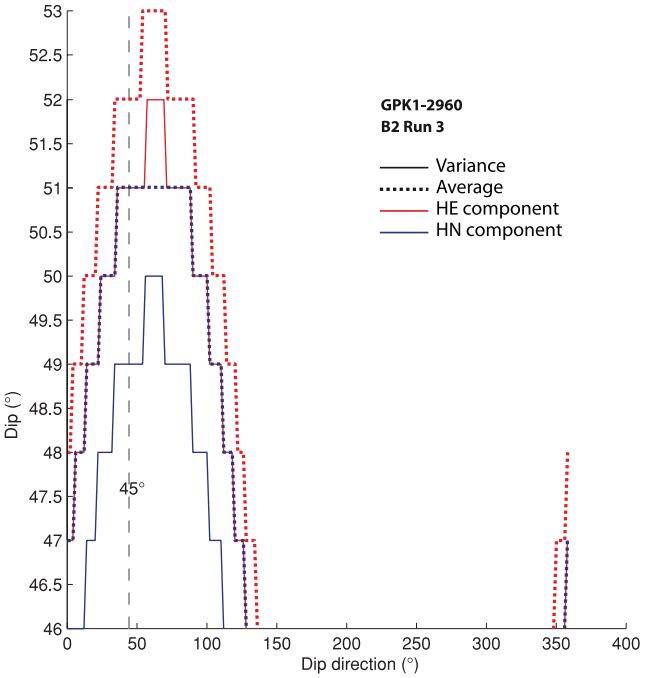

Figure A5. Arrival GPK1–2960: variance and average of the residuals (difference between modelled and observed traveltimes) in function of the orientation of the modelled reflector.

Other sources of structural information have to be taken into account to constrain the orientations. Because no coherent signal is detected on the other horizontal components, the azimuth of polarization cannot be used. Three main structures oriented N248°E 61°, N295°E 18° and N263°E 38° (Genter 1993) have been identified by borehole imaging. Only the first one is consistent with the curves in Fig. A4 and could correspond to the mean orientation of the fracture zone. Once again, it has to be mentioned that a single fracture identified by imagery is probably not perfectly representative of the orientation of a whole reflecting structure.

GPK1–2960 (∗)

Polarization analysis indicates that this arrival is polarized along the N045°E strike value, almost in a horizontal plane. Thus, this event is attributed to a *P*–*P* reflection according to the statements related to Fig. 5. Traveltime modelling from the two horizontal components of VSP B2 results in rather consistent minimum curves (Fig. A5). These curves have to be considered both at rather high dip value to ensure the almost horizontal polarization of the *P* reflected wave and at dip directions of N045°E and N225°E. Only the N045°E dip direction value may be regarded as a solution, inferring a dip value of 51°.

Fractures identified by imaging logs are oriented around the N265°E 85° mean value (Gentier *et al*. 2002), which is not consistent with the VSP results. This exemplifies again the discrepancy occurring between the orientation of a fault and the orientation of small-scale fractures.

GPK1–3090 (∗)

This arrival appearing on the vertical component (Fig. 4) is interpreted as a *P*–*S* reflection. A method similar to which has been applied to GPK1–2960 is also used in the present case: weak but distinguishable signals on the horizontal components combined to traveltime modelling allow us to derive low-confidence parameters for orientation (Table 1).

GPK1–3325 (∗)

The event is recorded on VSPs A3 run 1, C3 run 2 and D1 run 4 with very different time–depth curves, and both on vertical and horizontal components (Fig. 4). Modelling produces not very coherent results; however, results produced in the case of *P*–*P* reflections are better than the *P*–*S* case. Two different reflectors could explain the observed likely *P*–*P* arrivals with the same restricted quality (Table 1). Borehole imaging provides a value of N274°E 83° for a major fracture intersected by the well at this depth level (Gentier *et al*. 2002). If a coherency of orientation is assumed between this kind of fracture and the fracture zone as a whole, the value N260°E 63° derived from VSP should be preferred. In any case, the occurrence of energy both on vertical and horizontal components with a high discrepancy regarding their time–depth curves could be the signature of several arrivals (*P*–*P* and *P*–*S*) and justifies our special caution in discussing the results.